Journal of Materials Chemistry A

ROYAL SOCIETY OF CHEMISTRY

PAPER

View Article Online
View Journal | View Issue

Cite this: J. Mater. Chem. A, 2025, 13, 19605

MoO_x-based high-density nanoarrays on a substrate *via* smart anodizing as novel 3D electrodes for nano-energy applications†

Alexander Mozalev, *[a] Maria Bendova, [a] Lukas Kalina, [b] Jan Prasek, [ac] Francesc Gispert-Guirado [d] and Eduard Llobet [e]

Nanostructured molybdenum oxide (MoO_x) has many exciting properties that are highly dependent on the synthesis procedure. MoO_x nanostructures should be aligned on a substrate for nanoelectronic on-chip applications, which has been challenging. Here, for the first time, arrays of MoO_x-based nanoprotrusions of various morphologies (nanogoblets and nanorods), dimensions (20–500 nm), and surface densities (up to 10^{11} cm^{-2}), spatially separated and vertically aligned on a Si wafer, were synthesized *via* self-organized porous-anodic-alumina (PAA)-assisted anodization of a Mo underlayer covered with a few nm thick Nb interlayer. This creative anodization approach enabled sustainable growth of fully amorphous MoO_x within and under the PAA nanopores in several aqueous electrolytes, which other reported methods cannot accomplish. The nanoarrays grow *via* the outward migration of Mo^{n+} cations enabled by the thin niobium-oxide interlayer, followed by the concurrent migration of Mo^{n+} (n = 4–6) and Nb^{5+} cations in the PAA barrier layer and along the pore walls, competing with the migration of Mo^{n+} through the anodic molybdenum oxide that grows within the 'empty' pores. The nanorods derived after selective PAA dissolution feature a core/shell heterostructure: The shells are composed of MoO_3, several molybdenum suboxides (Mo^{5+}, Mo^{4+}), stoichiometric Nb_2O_5, and Al_2O_3, all mixed at the molecular level, whereas the cores are slightly hydrated and reduced MoO_3, as revealed by X-ray photoelectron spectroscopy. The annealing in air or vacuum at 550 °C increases the oxidation state of Mo^{n+} cations in the shells and causes the formation of monoclinic MoO_2 and orthorhombic Nb_2O_5 nanocrystallites in the bottom oxide. Mott–Schottky analysis disclosed n-type semiconductor properties of the cores, with the charge carrier density reaching 1×10^{22} cm^{-3}, whereas the shells seem more dielectric. The cyclic voltammetry and galvanostatic charge–discharge measurements featured characteristic reversible redox reactions, intensive electron transport, intercalation pseudocapacitive behavior, competitive charge-storage performance, and good rate capability of the rod's cores, which means the potential for nano-energy applications.

Received 13th April 2025
Accepted 19th May 2025

DOI: 10.1039/d5ta02921j

rsc.li/materials-a

1. Introduction

Molybdenum oxides (MoO_x) form a large group of materials based on the ability of molybdenum to possess various crystal structures, oxidation states, and local coordinations[1,2] giving rise to mixed-valency oxides. This incredible diversity results in a variety of electronic properties of MoO_x.[3] The stoichiometric anhydrous MoO_3 polymorphs (α-, β- and ε-phases) are nearly insulators. The almost stoichiometric $MoO_{3-\delta}$ (with $\delta < 0.03$), which retains the orthorhombic symmetry of α-MoO_3, the defective $MoO_{3-\delta}$ (with $0.03 < \delta < 0.11$), and the Magnéli phases are n-type semiconductors. The lower-valency cubic MoO_2, Mo_2O, and Mo_3O exhibit excellent metallic conductance.[3] The distinct lattice systems, valence states, and electronic properties of molybdenum oxides make their unique and highly diverse functionalities attractive for a wide range of energy conversion, energy storage, electro-optical, and electronic applications.[3–10] Nanoscale geometries have proved to be highly advantageous for further enhancing MoO_x functional properties due to enlarging the specific surface area and shortening charge carrier and ion diffusion pathways. The synthesis approaches involve gas-phase, solution-phase, thermal oxidation, and miscellaneous methods.[3] Although many

[a]Department of Microelectronics, Faculty of Electrical Engineering and Communication, Brno University of Technology, Technicka 10, 616 00 Brno, Czech Republic. E-mail: mozalev@vutbr.cz

[b]Institute of Materials Science, Faculty of Chemistry, Brno University of Technology, Purkynova 118, 612 00 Brno, Czech Republic

[c]CEITEC – Central European Institute of Technology, Brno University of Technology, Purkynova 123, 61 200 Brno, Czech Republic

[d]SRCiT, University Rovira i Virgili, Av. Paisos Catalans 26, 43007 Tarragona, Catalonia, Spain

[e]MINOS, University Rovira i Virgili, Av. Paisos Catalans 26, 43007 Tarragona, Catalonia, Spain

† Electronic supplementary information (ESI) available: Anodizing curves, SEM images, XPS- and XRD-related data, calculations, additional electrochemical data. See DOI: https://doi.org/10.1039/d5ta02921j

works have dealt with MoO_x-based nanodots, wires, tubes, flowers, platelets, spheres, or belts chaotically dispersed in solution or segregated on a substrate,[11] the formation of ordered and preferably self-assembled arrays of MoO_x nanostructures in geometries and arrangements beyond the reported ones, spatially separated and vertically aligned on substrates exhibits significant challenges, which arise because such protruding and ordered morphologies require precise control of the formation conditions, size, architecture, and position on the wafer scale. To date, such arrays have not been accomplished by either of the reported methods.[1,4] It is highly anticipated that the distinct separation and localization of charge carriers in arrays of well-defined, not agglomerating MoO_x nanocolumns, pillars, or rods will bring an effective synergy between the enlarged surface-to-volume ratio, enhanced surface reactivity, variable crystallinity, and electron conductivity of individual nanostructures in the arrays, which may be the missing building blocks for emerging on-chip electronic and nano-energy applications.[3,10,12]

To fill the gap, we propose an alternative solution-based approach to synthesize multi-dimensional MoO_x nanostructures highly ordered and vertically aligned on a substrate *via* smart anodizing of aluminum-on-molybdenum (Al/Mo) thin metal layers. The approach involves the growth of a porous anodic alumina (PAA) film immediately followed by anodizing the underlying Mo layer (hereafter 'PAA-assisted anodizing'),[13,14] all the electrochemical events occurring fully self-supportedly. The fundamental possibility of PAA-assisted anodizing was predicted theoretically and first justified experimentally by some of the present authors for Ti,[15] Ta,[16] and Nb.[13] Even though PAA-assisted nanostructures have recently been synthesized on several more valve metals,[17–21] there have been no reports on the PAA-assisted anodizing of Mo. The key challenge for preparing MoO_x by electrochemical techniques is the oxide's instability and the formation of highly soluble complexes with a wide range of anions.[22,23] This feature, complemented by oxide crystallization,[24] transpassivity,[25] suboxide formation tendency,[26] slow cation migration rate,[27] and an induction period revealed in anodic oxidation of Mo[28] makes direct PAA-assisted growth on Mo extremely challenging.

It is assumed that the equilibrium between oxide formation and dissolution may be controlled by mixing molybdenum oxide with some other metal oxides during anodic-oxide growth. As an option, Al_2O_3–MoO_x compounds might form due to the interaction of MoO_x with the alumina barrier layer and PAA cell walls through the PAA-assisted anodizing of molybdenum. Moreover, binary strong-interacting nanostructured oxides could grow during the PAA-assisted anodizing of molybdenum laminated with a layer of a different valve metal forming miscible components. Depending on the relative migration rate of Mo^{n+} ions in the mixture, even a minor addition of the second metal oxide might stabilize the composite.[29]

In the present work, we introduced a few-nm-thick interlayer of Nb between the Al and Mo layers, which were sputter-deposited onto a Si wafer. Such formed Al/Nb/Mo multilayer was anodized in several organic and inorganic acid electrolytes to tailor the balance between metal oxidation, oxide mixing, and oxide dissolution. Post-anodizing heat treatment was further employed to affect the composition, stoichiometry, and structure of the MoO_x-based mixed oxides. The new nanoarrays were examined using high-resolution scanning electron microscopy, advanced surface and structure analysis techniques, and electrochemical measurements. A model of the PAA-assisted oxide growth was proposed, linking ionic transport and interfacial phenomena in the films to the electrical and electrolytic formation conditions. The applicability of the arrays as 3D nanoelectrodes for on-chip supercapacitors was explored and discussed.

2. Experimental

2.1. Sample preparation

The precursor Al/Nb/Mo thin-film layers were prepared on thermally oxidized Si wafers by the magnetron sputter-deposition of a 170 nm thick Mo layer followed by a thin Nb layer and an 800 nm thick Al layer on top using Mo (99.95%), Nb (99.95%), and Al (99.9995%) targets (Kurt J. Lesker Company GmbH), respectively. The wafers with the deposited films were cut into *ca.* 1.5 cm × 1.5 cm pieces, which were anodized in a cylindrical top-open two-electrode electrolytic cell made of polytetrafluoroethylene, which secured the anodized area as a circle of 7.0 mm in diameter (0.4 cm^2). Further technical details of the anodizing setup are described elsewhere.[30]

Typically, the anodizing approach involved processing the Al overlayer in an aqueous acid solution to convert it into a PAA film, which was followed by the PAA-assisted re-anodizing of the Nb/Mo underlayers to a substantially higher voltage to achieve the growth of molybdenum and niobium anodic oxides within the PAA pores. Oxalic ($H_2C_2O_4$), sulphuric (H_2SO_4), phosphoric (H_3PO_4), and more exotic malonic [$CH_2(COOH)_2$],[31] tartaric [$(CH(OH)(COOH))_2$],[32] and etidronic [$CH_3C(OH)(PO_3H_2)_2$][33] acid solutions were probed as the anodizing electrolytes. The PAA layer formation was carried out galvanostatically at steady-state anodizing voltages ranging from 25 to 200 V, depending on the electrolyte. Selected samples were re-anodized to voltages relatively higher than the steady-state values established during the PAA growth in 0.5 M H_3BO_3 and 0.05 M $Na_7B_4O_7$, pH 7.5 (hereafter, 'borate buffer'). Finally, the PAA overlayers were dissolved in a chemical solution prepared and used as described elsewhere (hereafter, 'selective etchant'),[34,35] rinsed in ultrapure water, and dried in a cool nitrogen stream.

Following re-anodizing, selected samples were annealed at 550 °C for 3 hours either in ambient air at atmospheric pressure (hereafter '*air-annealed*' samples) or at a residual pressure of 10^{-5} Pa (hereafter '*vacuum-annealed*' samples).

2.2. Analysis and measurements

Scanning electron microscopy (SEM) observation of surfaces and cross-sections of the anodic films before and after the PAA dissolution was performed in a TESCAN MIRA II field-emission instrument operated at 15 or 30 kV accelerating voltage and in an FEI Verios 460L SEM operating in immersion mode at 15 kV accelerating voltage and 0.8 nA probe current. No conducting layers were deposited over the sample surfaces before observation. For statistical analysis, the surface SEM images were analyzed using ImageJ software.

X-ray photoelectron spectroscopy (XPS) analysis was conducted in a Kratos Axis Ultra DLD spectrometer and a Kratos Axis Supra spectrometer using a monochromatic Al Kα source with an X-ray emission power of 75 or 150 W and typical operating pressures less than 1.3×10^{-9} mbar. The X-ray beam was focused to a 300 μm × 700 μm spot. The emitted electrons were detected at fixed pass energies of 160 eV for the survey spectra and 20 eV for the high-resolution spectra. The Kratos charge neutralizer system was used for all measurements. The software for spectra analysis was CasaXPS version 2.3.17. GL(30) profiles were used for all components except the metallic core lines of Nb 3d, for which asymmetric profiles LA(1.2, 3.3, 12) were applied. All spectra have been charge-corrected to give the adventitious C 1s spectral component (C–C, C–H) binding energy of 284.8 eV. The quantitative analysis was performed from the high-resolution spectra using the relative sensitivity factors from CasaXPS suitable for Kratos Axis spectrometers, referenced to F 1s. Further details are described elsewhere.[13,36,37]

X-ray diffraction (XRD) patterns of the as-formed and annealed anodic films were taken from a Bruker-AXS D8-Discover diffractometer operated at 40 kV and 40 mA to generate CuKα radiation. An X-ray collimator of a 500 μm system was used. The VÅNTEC-500 detector (silicon strip technology, active area of 30 cm × 30 cm, frame size of 2048 pixels × 2048 pixels) was placed at a 15 cm distance from the sample. Sixteen frames were collected in reflection mode covering 20–90° 2θ with a step size of 0.8° to obtain a conventional 2D diffractogram suitable for Rietveld analysis.[38] The exposure time was 300 s per frame, and it was γ-integrated to generate the 2θ *vs.* intensity diffractogram. The experimental diffractograms were fitted with the crystal structure[39] for the phases identified using TOPAS 6.0 software (Bruker AXS GmbH, 2017).[40]

Electrochemical impedance spectroscopy (EIS), cyclic voltammetry (CV), and galvanostatic charge–discharge (GCD) measurements were carried out in the borate buffer at 22 °C using an Autolab PGSTAT204 Potentiostat/Galvanostat with a FRA32M module (Metrohm). A cylindrical PTFE cell secured the measured area of 0.25 cm^2 for all electrochemical measurements. A three-electrode setup comprising the sample as the working electrode, an Au plate as the counter electrode, and an Ag/AgCl (1 M KCl) as the reference electrode was used in all measurements. The CV was typically performed between −1.9 and −0.1 V *vs.* Ag/AgCl with a scan rate of 50 mV s^{-1} starting from the open-circuit potential (OCP) of around −0.3 V *vs.* Ag/AgCl in the anodic direction to −0.1 V *vs.* Ag/AgCl, followed by one cathodic and one anodic sweeps. Experimental details of GCD, EIS, and Mott–Schottky measurements are given in the ESI.† Unless stated otherwise, all area-related physical quantities were related to the apparent surface area exposed to anodization or electrochemical measurements.

3. Results and discussion

3.1. Formation, characterization, and modeling

3.1.1. Anodizing behavior. As an example, Fig. 1a shows the recorded voltage–time and current–time responses during the anodizing of an Al(800 nm)/Nb(25 nm)/Mo(170 nm) trilayer in

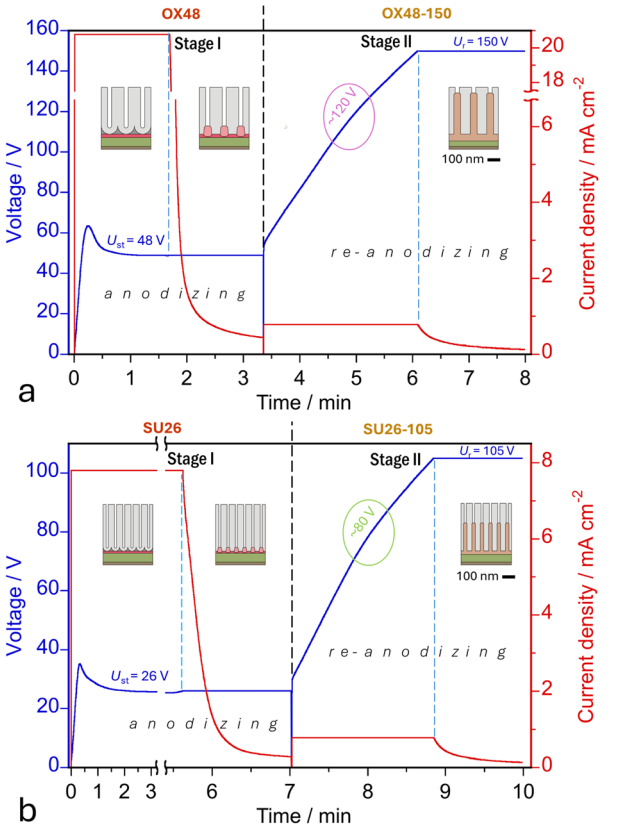

Fig. 1 Voltage–time and current–time responses during: (a) the anodizing in 0.6 M $H_2C_2O_4$ (stage I) followed by re-anodizing in 0.5 M H_3BO_3 and 0.05 M $Na_7B_4O_7$ (borate buffer) (stage II) of Al(800 nm)/Nb(*25 nm*)/Mo(170 nm) metal layers; (b) the anodizing in 0.2 M H_2SO_4 (stage I) followed by re-anodizing in the borate buffer (stage II) of Al(800 nm)/Nb(*15 nm*)/Mo(170 nm) metal layers for forming two characteristic types of nanoarrays differing in sizes and geometries, as suggested in the embedded schematics. The samples are coded according to the anodizing acid and steady-state anodizing voltage, U_{st}, at stages I (OX48 and SU26) and the final re-anodizing voltage, U_r, at stages II (OX48-150 and SU26-105).

0.6 M oxalic acid at a constant-current density of 21 mA cm^{-2}, resulting in a steady-state PAA formation voltage U_{st} = 48 V, followed by 1 min potential hold after the anodizing front reaches the Al/Nb interface (stage I). The anodizing voltage–time curve seems typical for PAA growth in oxalic acid electrolytes at moderate current densities without abnormalities.[41–44] Despite the small thickness of the aluminum layer, steady-state PAA growth is attained. This underlines the quality of the aluminum layer prepared *via* the magnetron sputter deposition. Once the anodizing front reaches the Nb underlayer, the voltage begins to increase, and the process is automatically switched to potentiostatic mode.[16] The beginning of voltage rise indicates the start of local anodic oxidation of the Nb/Mo bilayer, which is associated with the formation of niobium oxide and its penetration into the PAA barrier layer. Analysis of the current decay during the potential hold does not reveal any significant deviations from the usual current–time behavior during the PAA-assisted anodizing of valve metals, specifically Nb, previously reported.[13,16] Nevertheless, the dot-like oxidation of the Mo underlayer may begin before the end of stage I.

The PAA-assisted re-anodizing is carried out following a break to rinse and dry the pores after the anodizing. It is performed in the borate buffer galvanostatically under a low current density of 0.8 mA cm^{-2} until the re-anodizing voltage, U_r, reaches the set value (150 V), followed by a potential hold over 60 s (stage II). One may see that the voltage rise begins to retard at about 120 V. With reference to early works on compact anodizing of thin-film multilayers,[45,46] it is assumed that the Nb interlayer is nearly fully transformed into anodic oxide and further anodizing consumes merely the Mo underlayer. The behavior appeared typical for all samples anodized in the oxalic acid and re-anodized up to the maximum voltage of 306 V (as shown in Fig. S1a and b†), at which dielectric breakdown interrupts the normal film growth. The Al(800 nm)/Nb(**25 nm**)/Mo(170 nm) trilayer anodized in the oxalic acid at $U_{st} = 48$ V to the end of stage I will be coded OX48; the same samples re-anodized to $U_r = 150$ V till the end of stage II will be coded OX48-150. The digit after the dash will change accordingly if the sample was re-anodized to a different final U_r value.

Fig. 1b shows an example of the voltage–time and current–time responses of the Al(800 nm)/Nb(15 nm)/Mo(170 nm) trilayer during galvanostatic anodizing in 0.2 M H_2SO_4 at 8.0 mA cm^{-2} followed by galvanostatic re-anodizing in the borate buffer at 0.8 mA cm^{-2} up to 105 V, both processes finishing with short potential holds. The anodizing responses show that the steady-state pore growth is established at 26 V, as one may expect for mild aluminum anodizing in 0.2 M H_2SO_4 at a low current density without initiating any specific effects.[47] The re-anodizing voltage–time curve changes its slope at about 80 V, generally exhibiting the same tendency as in Fig. 1a. The lower voltage at which the slope changes is explained by the thinner Nb interlayer (15 *vs.* 25 nm). The Al(800 nm)/Nb(**15 nm**)/Mo(170 nm) trilayer anodized in the sulphuric acid at $U_{st} = 26$ V to the end of stage I will be coded SU26; the same samples re-anodized to $U_r = 105$ V till the end of stage II will be coded SU26-105. The schematics in Fig. 1 suggest preliminary views of the film structures expected at the end of the corresponding stages, which will later be updated based on SEM observations.

3.1.2. SEM observation. Fig. 2a–d shows SEM images of fragments of the OX48 sample before and after the PAA dissolution. The PAA surface is microscopically smooth, populated with regularly dispersed tiny depressions, which are pore outlets. An array of nanosized goblet-like nanostructures penetrating the PAA barrier layer is observed in the cross-section in Fig. 2c. Fig. 2d shows a 3D view of what remains on the substrate after the PAA dissolution. The goblets grow above

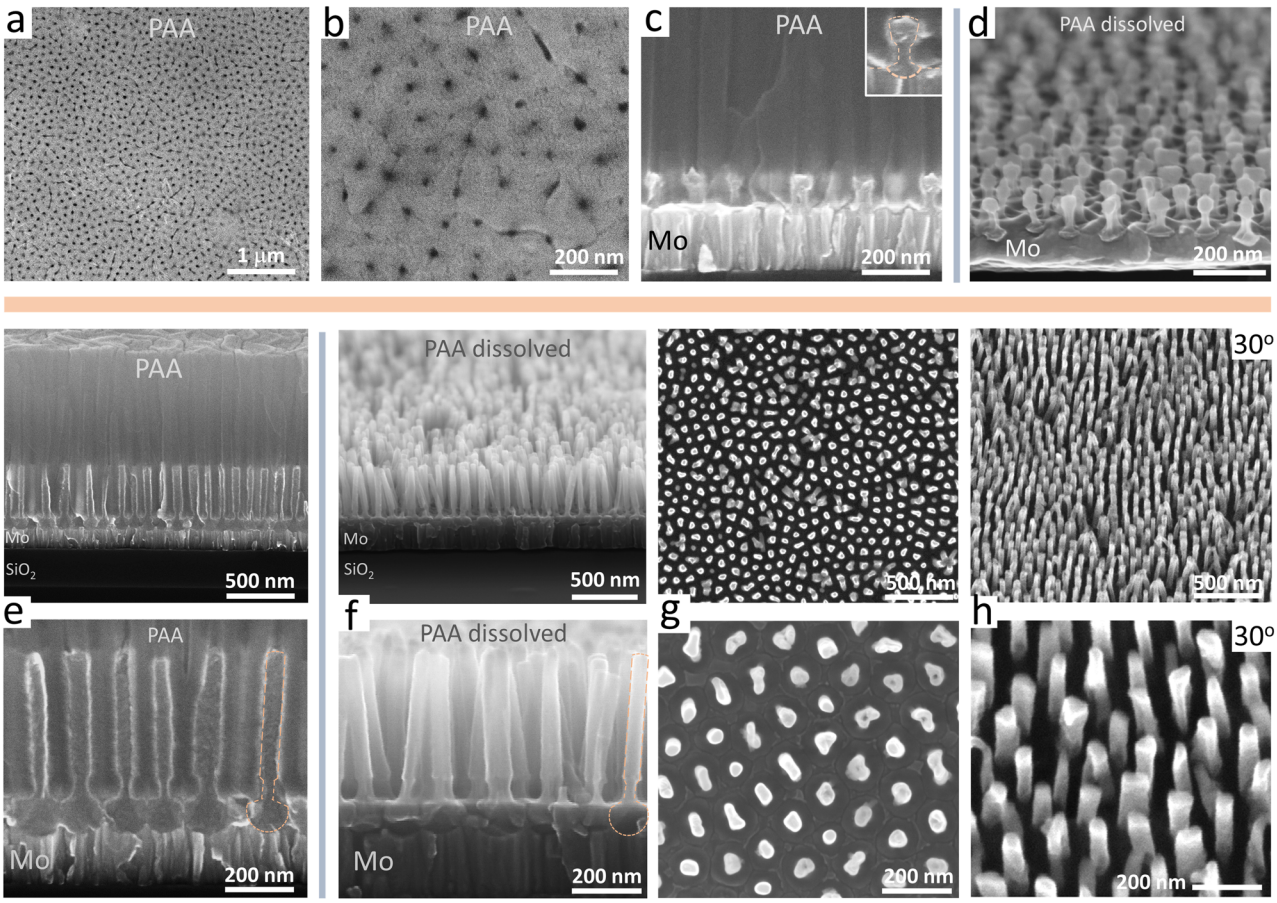

Fig. 2 Surface, cross-sectional, and 3D SEM views of nanostructured anodic films made by (a–d) the anodizing of Al(800 nm)/Nb(25 nm)/Mo(170 nm) metal layers in 0.6 M oxalic acid at $U_{st} = 48$ V (coded as OX48, Fig. 1a) followed by (e–h) the re-anodizing in borate buffer to $U_r = 180$ V (coded as OX48-180, as in Fig. 1a). The images in (d, f, g and h) were recorded after dissolving the porous anodic alumina (PAA) layer in a selective etchant[35] (PAA-free samples).

the former Al/Nb interface while their plates are embedded in the metal below the mentioned interface (hereafter the '*bottom layer*'), marked with the dashed lines in the inset of Fig. 2c. The definition of the bottom layer is described in detail elsewhere.[48,49]

The lower panel of Fig. 2 shows cross-sections and surfaces of the OX48-180 sample before and after the PAA dissolution. To an extent, the re-anodizing procedure lengthens the oxide protrusions inside the pores. An array of rod-like nanostructures rising to about 405 nm above the film surface, spatially separated and vertically aligned on the substrate, is derived after the PAA dissolution (Fig. 2f). As seen in Fig. 2f, the goblets' roots widen, and the bottom-oxide parts further expand into the underlying molybdenum metal, invading more space and forming nanoballs touching each other such that the balls form a continuous layer, 100 nm thick, buffering the protruding parts from the remaining Mo metal. In both samples (Fig. 2d and f–h), the measured population density of the protrusions is 8×10^9 cm^{-2}, which corresponds well to the theoretical number of pores in the PAA overlayer. From the statistical analysis of the surface images of samples re-anodized to various voltages up to 220 V, the mean diameter of the rods is 50 nm regardless of the U_r-value, which is 1.7 times the average pore size in the PAA film (29 nm).

The definition and shifts of the principle interfaces in the OX48 and OX48-180 samples are elaborated in the cross-sectional SEM images in Fig. S2.† The development of the oxide nanorods and their bottom layers with increasing U_r is demonstrated in Fig. S3† with the help of frontal SEM views of the OX48-based samples re-anodized to various U_r ranging from 150 to 220 V. The lines drawn over the images indicate the depths of the bottom layers and the rods' lengths within the pores. The SEM observations and measurements for the OX48-based samples shown in Fig. 2 and S2, S3,† complemented by the XPS and XRD data analyses, create the basis for understanding the ionic transport and mechanism of oxide growth, which will be discussed in Section 3.1.5.

Several other organic and inorganic acid electrolytes, commonly or rarely used for PAA formation, have also been tried in this work, with the best results achieved to date in 0.2 M H_2SO_4 and 0.2 M H_3PO_4 aqueous solutions. Fig. 3 shows selected SEM images of cross fractures and surfaces before and after PAA dissolution of the Al/Nb/Mo multilayers anodized/re-anodized in 0.2 M sulphuric acid/borate buffer (sample SU26-105) and 0.2 M phosphoric acid at $U_{st} = 150$ V following the anodizing approach described in our previous works (Fig. S1c†).[17,50] In the case of sulphuric-acid anodizing, the thickness of the Nb interlayer was 15 nm to involve molybdenum in the oxidation process more substantially. From SEM observation of the SU26-105 sample (Fig. 3a–c), the PAA-assisted anodizing generates arrays of tiny rod-like nanostructures of the highest population density of 3×10^{10} cm^{-2}, about 20 nm wide, 220 nm long, and supported by an array of semispherical bottom-oxide regions in the remaining Mo metal layer. Alternatively, the goblet-like protrusions generated *via* the PAA-assisted anodizing/re-anodizing in the phosphoric acid (Fig. 3d–f) appear proportionally bigger, exhibiting the lowest population density of 7×10^8 cm^{-2}. The mean center-to-center distance of 400 nm measured in this sample is the longest achieved by the approach developed in this work.

Based on the SEM examination of various samples, we selected the nanoarrays synthesized in the oxalic acid (the

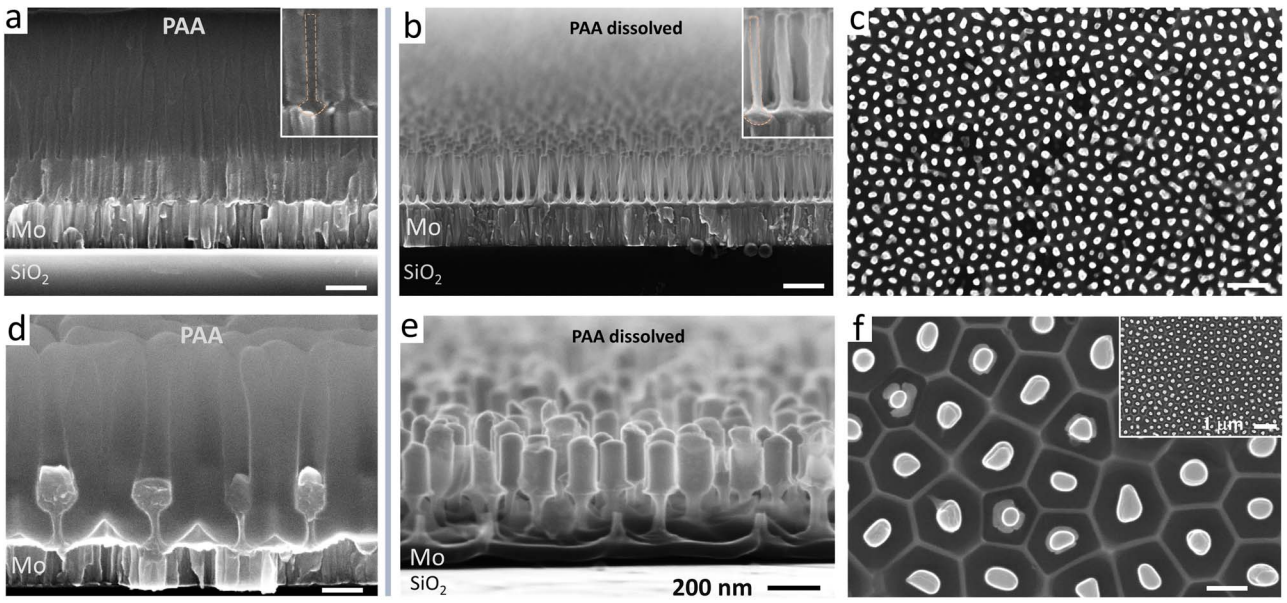

Fig. 3 Surface and cross-sectional SEM views of nanostructured anodic films made by (a–c) the anodizing of Al(800 nm)/Nb(15 nm)/Mo(170 nm) metal layers in 0.2 M sulphuric acid at $U_{st} = 26$ V followed by the re-anodizing in the borate buffer to $U_r = 105$ V, as in Fig. 1b, and (d–f) the anodizing of Al(800 nm)/Nb(25 nm)/Mo(170 nm) metal layers in 0.2 M phosphoric acid at $U_{st} = 150$ V followed by re-anodizing to $U_r = 160$ V, as shown in Fig. S1c.† The images in (b, c, e and f) were recorded after dissolving the PAA layers in the selective etchant (PAA-free samples). The unlabelled scale bars are 200 nm.

OX48-based films) as model systems for carrying out chemical and structural analyses and investigating the cooperative ionic transport during the PAA-assisted oxide growth on the superimposed Nb and Mo thin film layers.

3.1.3. Chemical composition. The chemical composition and bonding states in the surface layer of the as-anodized OX48, as-reanodized OX48-220, and air- and vacuum-annealed OX48-220 nanostructured films derived after or before the PAA dissolution were investigated by XPS (Fig. 4 and 5). C, O, Nb, Mo, Al, P, and Cr were identified in all samples' survey spectra. P and Cr were adsorbed from the selective etching. Hereafter, the samples from which the PAA layer was fully dissolved away before XPS analysis will be referred to as 'PAA-free'. In the case of a partial PAA dissolution to expose the oxide protrusions while keeping the bottom layer covered with the remaining PAA layer (as depicted in the ESI†), the samples will be distinguished as 'PAA-half-etched' films. In contrast, the as-prepared anodized and re-anodized samples will be mentioned as 'PAA-inbuilt' films.

Narrow-scan C 1s, O 1s, Mo 3d, Nb 3d, and Al 2p spectra were collected to analyze the elements' core levels and bonding states. The experimental and fitted Mo 3d, Nb 3d, and Al 2p spectra of selected OX48-220-based films are shown in Fig. 4 and 5. Spectra of the other samples are presented in the ESI† (PAA-free OX48-180, PAA-free OX48-15 nm Nb-based, and PAA-half-etched OX48-220-based films, Fig. S5 and S6†), including the details of deconvoluting the Mo 3d spectra, also considering the Nb 3d loss peaks partially overlapping with the Mo 3d transitions (Fig. S4†).

The analysis of Mo 3d spectra of all the OX48-based films (left columns in Fig. 4 and S5, S6†) was complicated by a substantial contribution of Nb 3d loss peaks partially overlapping with the Mo 3d transitions because the Mo : Nb ratio was relatively low (<25 at% Mo, provided that at%(Nb + Mo) =

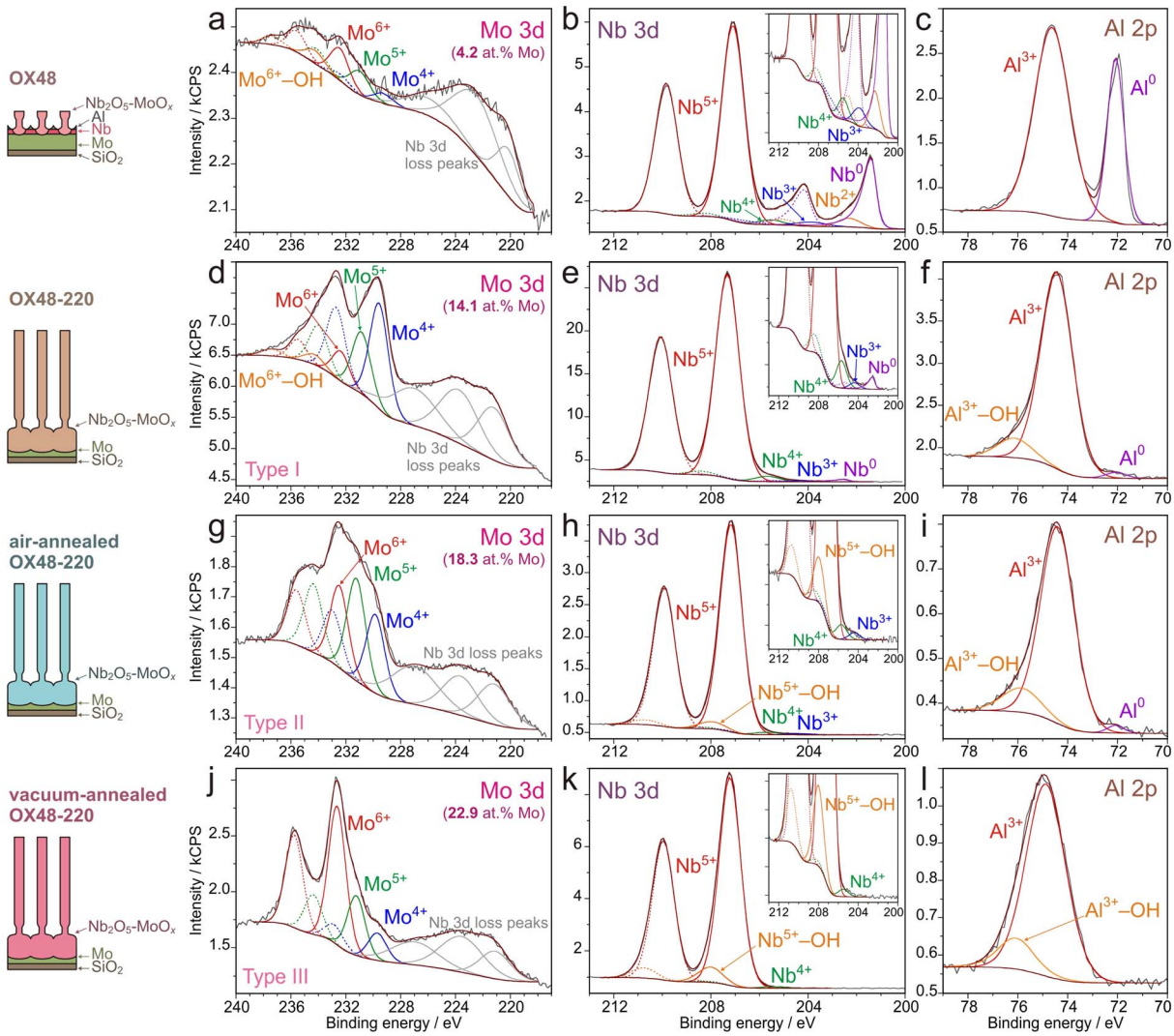

Fig. 4 Experimental and curve-fitted narrow-scan (left column) Mo 3d, (middle) Nb 3d, and (right) Al 2p XP spectra of the (a–c) OX48, (d–f) OX48-220, (g–i) air-annealed OX48-220, and (j–l) vacuum-annealed OX48-220 samples. The sample codes and formation conditions are defined in Fig. 1 and 2. The PAA layers were dissolved in the selective etchant before the XPS analysis. The peak positions, FWHMs, and at% are summarized in Table S1.†

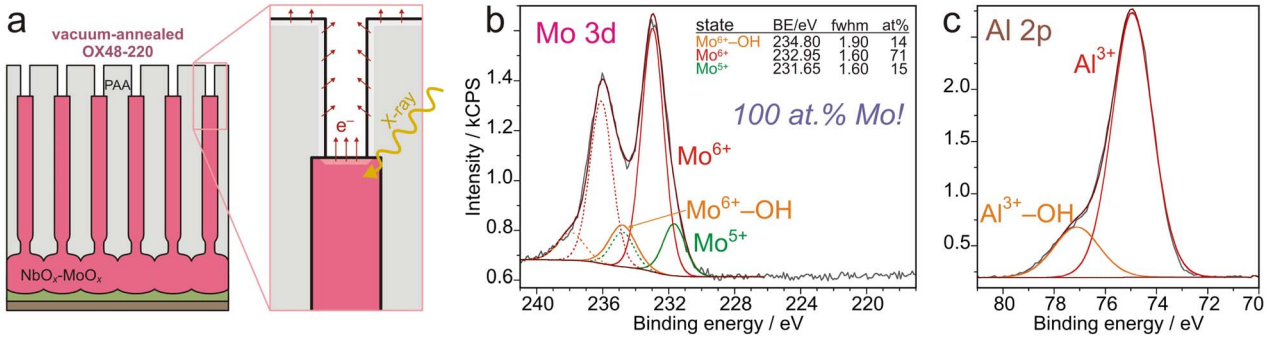

Fig. 5 (a) Schematics and (b and c) experimental and curve-fitted narrow-scan (b) Mo 3d and (c) Al 2p XP spectra of the vacuum-annealed PAA-inbuilt OX48-220 sample.

100 at%). The detailed procedure of adding Nb 3d loss peaks while maintaining a constant Nb-3d-loss-to-Nb-3d ratio of 0.175 ± 0.02 is described in the ESI.† The Mo 3d transitions are fitted with $3d_{5/2}$–$3d_{3/2}$ doublets with a constrained spin–orbit splitting of 3.13 eV, fixed intensity ratio $3d_{5/2}:3d_{3/2}$ of 3 : 2, and a full width at half maximum (FWHM) equal for $3d_{5/2}$ and $3d_{3/2}$ components.

Up to four Mo 3d doublets reproduce each spectrum, with Mo $3d_{5/2}$ at 232.4 ± 0.2, 231.0 ± 0.2, 229.6 ± 0.2, and 234.3 ± 0.2 eV, with variable individual contributions to each spectrum. Based on the literature reports,[51–53] we assign the doublet at 232.4 eV (Mo $3d_{5/2}$) to Mo^{6+} cations in MoO_3. The lowest-binding-energy (BE) doublet at 229.6 eV (Mo $3d_{5/2}$) is assigned to Mo^{4+} cations in MoO_2. The highest-BE doublet at 234.3 eV (Mo $3d_{5/2}$), identified in the spectra of the as-prepared films, is associated with Mo^{6+}–$OH(H_2O)$ coordination. Last, the doublet at 231.0 eV (Mo $3d_{5/2}$) may be assigned to Mo^{5+} cations in Mo_2O_5. The various oxides are assumed to be mixed at the molecular level, which may be expressed as $Mo^{VI}_{y1}Mo^{V}_{y2}Mo^{IV}_{y3}O_{x1}(OH)_{x2}$ and vary in the different parts of the anodic films, such as the rods and the bottom oxide.

The dissimilarities in the recorded Mo 3d spectra of the PAA-free films reflect the differences in the content of the individual Mo^{n+} species. Three characteristic types of MoO_x (marked in Fig. 4d, g and j) can be distinguished: type I – 'highly reduced' MoO_x, which comprises a dominating amount of Mo^{4+} cations, is characteristic of the re-anodized as-prepared films (Fig. 4d, left column in Fig. S5†). Type II – 'moderately reduced' MoO_x, which comprises Mo^{6+}, Mo^{5+}, and Mo^{4+} cations in comparable concentrations, is associated with the air-annealed film (Fig. 4g). Type III – 'slightly reduced' MoO_x, which contains a dominating amount of Mo^{6+} cations, is linked to the vacuum-annealed film (Fig. 4j and 5b). The average values of oxidation state for Mo ions in the oxide types are 4.73 ± 0.1 (type I, six samples), 4.98 ± 0.1 (type II, four samples), and 5.40 ± 0.1 (type III, six samples), beside the vacuum-annealed PAA-inbuilt film, which revealed the presence of almost pure MoO_3 (Fig. 5b).

The Mo 3d pattern of the PAA-free OX48 sample (Fig. 4a) cannot be analyzed precisely because of a low Mo content (4.2 at%, providing that at%(Nb + Mo) = 100%, calculated after subtracting the metallic contributions from the Nb 3d spectrum, as will be shown later). The PAA-free OX48-220 sample, which is a reference for comparison with the other samples, comprises type I MoO_x (Fig. 4d). Re-anodizing to a relatively low $U_r = 180$ V (OX48-180) or employing a thinner (15 nm) Nb interlayer in the Al/Nb/Mo trilayer (coded as OX48-220-15 nm Nb) does not alter the MoO_x pattern (left column in Fig. S5†). However, when the half-etched PAA covers the roots of the OX48-220 nanorods and the bottom oxide, type II MoO_x is revealed (Fig. S6a†). Since the bottom oxide is unreachable for the XPS analysis in the PAA-half-etched sample and only the rods emit photoelectrons, the nanorods' outer layer is assumed to be more oxidized than the bottom oxide. Moreover, all re-anodized OX48-based samples contain 5–10% of hydroxylated MoO_3, which may be expressed as $MoO_{3-x}(OH)_{2x}$.

The quantitative analysis shows that Mo content in the four various re-anodized PAA-free OX48-based films (see Table 1 and left column of Fig. S5†) ranges between 11.5 and 15.5 at% (provided that at%(Nb + Mo) = 100%). It increases slightly with increasing re-anodizing voltage or thinning Nb interlayer. The PAA-half-etched OX48-220 surface reveals a substantially higher Mo content of 19.3 at%, assuming compositional differences in the various film parts, with more molybdenum oxide in the rods' surface than in the bottom oxide.

Comparative analysis of Mo 3d spectra of the PAA-free *air- and vacuum-annealed* OX48-220 films (Fig. 4g, j and Table 1) assumes that MoO_x is more oxidized in the annealed films (type II and III) than in the as-prepared film (Fig. 4d, type I). Furthermore, the highest degree of MoO_x oxidation (type III) is noted in the vacuum-annealed sample. The two annealed films also show higher Mo content than the as-prepared sample. The air-annealed PAA-half-etched sample (Fig. S6g†), where only the rods are PAA-free, not the bottom layer, reveals relatively more oxidized MoO_x and a higher overall Mo content compared with its PAA-free counterpart (Fig. 4g). Furthermore, the air and vacuum-annealed films do not contain $MoO_{3-x}(OH)_{2x}$.

The most stunning effect is noted in the vacuum-annealed PAA-inbuilt sample, in which only the rods' tops and the PAA surface emitted photoelectrons, as shown in Fig. 5a. Here, 100 at% Mo is associated with slightly reduced and hydrated MoO_3, assuming that the entire inner oxide composing the rods is MoO_x with no additions of Nb_2O_5. The inner oxide comprises

Table 1 Quantitative results of the XPS analysis of various anodic films prepared in this study

Film code	State of PAA dissolution	Mo content (at%) (at%(Nb + Mo) = 100 at%)	Average ox. state of Mo/type	Amount of Nb^{n+} (n = 3 and/or 4) (%)	Al content (at%) (at%(Al + Nb + Mo) = 100 at%)	Figure
OX48	PAA-free	4.2	5.45/?	5.3	24	Fig. 4a–c
OX48-180	PAA-free	11.5	4.81/I	2.1	56	Fig. S5a–c
OX48-220	PAA-free	14.1	4.67/I	3.2	54	Fig. 4d–f and S5d–f, S6d–f
	PAA-half-etched	19.3	5.13/II	0	97	Fig. S6a–c
OX48-180-15 nm Nb	PAA-free	12.6	4.63/I	5.2	54	Fig. S5g–i
OX48-220-15 nm Nb	PAA-free	15.5	4.88/I	2.1	51	Fig. S5j–l
Air-annealed OX48-220	PAA-free	18.3	5.00/II	1.9	60	Fig. 4g–i and S6j–l
	PAA-half-etched	22.4	5.39/III	0	85	Fig. S6g–i
Vacuum-annealed OX48-220	PAA-free	22.9	5.49/III	0.7	42	Fig. 4j–l
	PAA-inbuilt	100	5.85/III	n/a	96	Fig. 5b and c

a small amount of $MoO_{3-x}(OH)_{2x}$, which cannot be detected when the whole surface of the PAA-free films is exposed to the analysis.

The location of various types of MoO_x and the differences in the overall Mo content (when at%(Nb + Mo) = 100%) over the various parts of the OX48-220 samples (as-prepared, air-annealed, and vacuum-annealed) are depicted in Fig. 6.

To summarize the Mo 3d peak analysis, the surface of the oxide nanorods comprises relatively more oxidized MoO_x (type II or III, about 20 at% Mo), whereas the bottom-oxide's surface contains less-oxidized MoO_x, most likely MoO_2 (about 5 at% Mo), and is enriched with Nb_2O_5. The oxide composing the nanoballs of the bottom layer (Fig. 6) contains no niobium oxide but reduced MoO_x, likely MoO_2. The interior of the rods is slightly reduced MoO_3 mixed with a minor amount of $MoO_{3-x}(OH)_{2x}$ without any addition of Nb_2O_5.

The Nb 3d spectra of all OX48-based films (middle columns in Fig. 4 and S5, S6†) are fitted with Nb $3d_{5/2}$-$3d_{3/2}$ doublets with a constrained spin–orbit splitting of 2.75 eV, fixed intensity ratio $3d_{5/2}:3d_{3/2}$ of 3 : 2, and a FWHM equal for the $3d_{5/2}$ and $3d_{3/2}$ components. All the spectra contain a dominant doublet with Nb $3d_{5/2}$ component at 207.18 ± 0.15 eV, associated with Nb^{5+} cations in Nb_2O_5.[13,36,49] For most of the films, several low-intensity doublets are added with Nb $3d_{5/2}$ at 205.54 ± 0.15, 204.25 ± 0.2, 202.2 ± 0.3, and 208.03 ± 0.1 eV, which are assigned to Nb^{4+}, Nb^{3+}, Nb^0, and Nb^{5+}–OH/H_2O coordinations, respectively.[13,36,49] Thus, the surface of the PAA-free OX48 film (Fig. 4b) contains a dominating amount of Nb_2O_5 mixed at the molecular level with a minor amount (5%) of Nb^{4+}- and Nb^{3+}-based suboxides, while some metallic residues remain between the bases of the nanoprotrusions (Nb^0 and Nb^{2+} cations, ~20% of all Nb species in the spectrum). Notably, the metallic Mo^0 peak is not present in the corresponding Mo 3d spectrum (Fig. 4a) because the unoxidized Mo is buried under the residues of the 25 nm thick Nb network. The four PAA-free OX48-based films, made by re-anodizing the Al/Nb(25 nm)/Mo or Al/Nb(15 nm)/Mo trilayers to 180 or 220 V (Fig. 4e, middle column in Fig. S5†), also contain Nb_2O_5 mixed with a low amount of suboxides (2–5%, a summary is available in Table 1). A minor amount of metallic niobium (0.5–7%), further decreasing with increasing re-anodizing voltage, is noted. A substantial change is observed for the PAA-half-etched OX48-220 film (Fig. S6b†), where the rods emit photoelectrons but not the bottom oxide. This surface features the presence of stoichiometric Nb_2O_5 and the absence of metallic residues. This means that the Nb suboxides detected in the PAA-free films reside in the bottom-oxide layer, not in the rods, and the remaining PAA layer masks the metallic residues.

The PAA-free *air- and vacuum-annealed* OX48-220 samples (Fig. 4h and k), similarly to their as-prepared counterpart (Fig. 4e), contain a dominating amount of Nb_2O_5 mixed with NbO_2 and Nb_2O_3 (<2 at%). There are no metallic Nb^0 peaks in the spectra. Considerable amounts of hydroxylated Nb_2O_5 are present in the annealed films, with Nb^{5+}–OH/H_2O coordination of ~7%, which can be expressed as $Nb_2O_{5-x}(OH)_{2x}$. Therefore, the two annealed surfaces become more oxidized. Paradoxically, the vacuum-annealed surface appears more oxidized than the

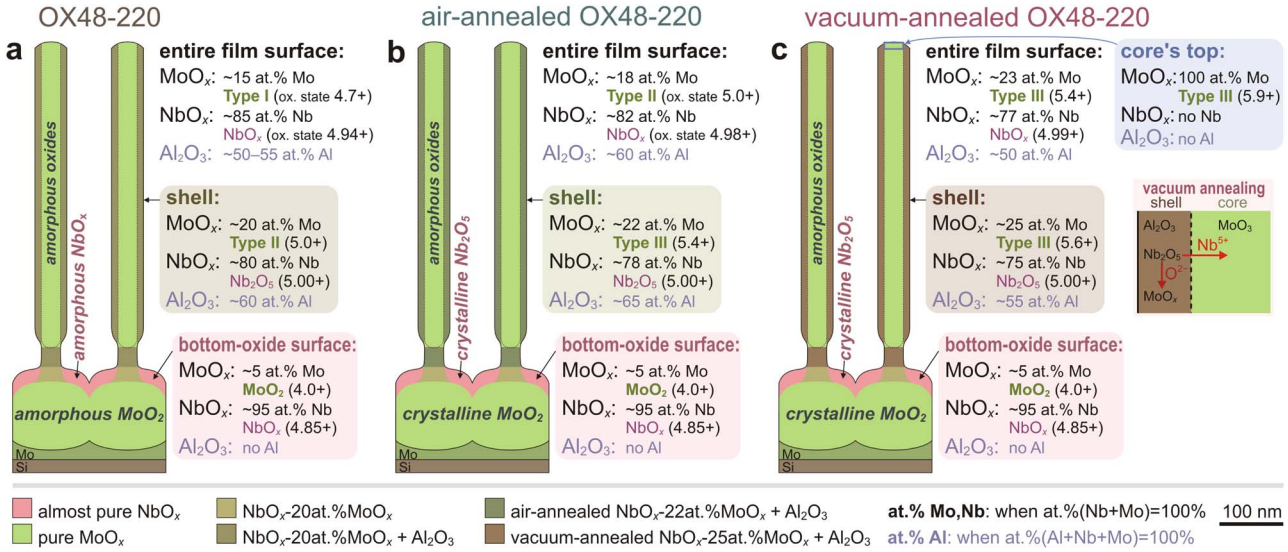

Fig. 6 Schematic cross-sectional views visualizing the XPS and XRD results for the (a) as-prepared (as in Fig. 1 and 2), (b) air-annealed (550 °C, 3 h, atmospheric pressure), and (c) vacuum-annealed (550 °C, 3 h, 10^{-5} Pa) OX48-220 samples.

air-annealed one, which agrees with the trend observed for the MoO_x. When the half-etched PAA covers the bottom oxide in the air-annealed film, the Nb 3d spectrum (Fig. S6h†) has no sub-oxide peaks, meaning that the suboxides reside in the bottom oxide, not in the rods, similar to the as-prepared sample. However, the Nb^{5+}–OH/H_2O coordination (6%) is identified in the Nb 3d spectrum of the air-annealed PAA-half-etched sample in a larger amount than in the PAA-free sample (4%). This implies that the rods' surface accommodates hydroxylated Nb_2O_5, not the bottom oxide.

The Al 2p spectra of the OX48-based samples (right columns in Fig. 4 and S5, S6†) are relatively simple and are all fitted with up to three symmetrical peaks associated with Al_2O_3 (74.63 ± 0.3 eV, dominating amount), Al^0 (72.08 ± 0.05 eV), and Al^{3+}–OH (76.00 ± 0.15 eV). The surface layer of the PAA-free OX48 (Fig. 4c) contains ~30 at% Al^0, in addition to Al_2O_3. The presence of metallic Al is due to the network of non-anodized aluminum around the oxide nanoprotrusions. The Nb^0 doublet in the corresponding Nb 3d spectrum has the same origin (Fig. 4b). The metallic contributions to the Nb 3d and Al 2p spectra were subtracted from the overall content of the elements to obtain an approximate surface concentration of Al^{3+} in the anodic parts of the film. The corresponding native alumina, covering the Al^0 network, was also considered and subtracted.[54] Provided that at%(Al + Nb + Mo) = 100%, the surface of the oxide nanorods in the anodized sample contains 24 at% Al (Al^{3+}).

The Al 2p spectra of the four PAA-free as-reanodized OX48-based films (Fig. 4f, right column in Fig. S5†) contain the three peaks associated with a dominating amount of Al_2O_3 and minor amounts of Al^{3+}–OH coordination (10–15 at%) and Al^0 (1–5 at%). The contribution of Al^0 decreases with increasing re-anodizing voltage from 180 to 220 V. The amount of Al in the surface layer of the PAA-free as-reanodized films is 50–55 at% (when at%(Al + Nb + Mo) = 100%). This finding agrees with previous reports on several PAA-assisted nanostructures (N-doped TiO_2,[55] Se-doped Nb_2O_5,[49] and Se-doped ZrO_2)[35] containing 50 to 80 at% Al in the form of Al_2O_3.

The PAA-half-etched OX48-220 sample (Fig. S6c†) ontains Al_2O_3 only. The Al^0 peak is absent in the spectrum since the underetched PAA covers the aluminum residues. The absence of Al^{3+}–OH coordination implies that the hydroxylated Al_2O_3 resides in the rods' roots. The deep-laid bottom oxide is supposed to be alumina-free because it forms merely by the inward migration of O^{2-} anions.

The Al 2p spectra of the PAA-free annealed OX48-220 films (Fig. 4i and l) also contain the Al^{3+}–OH peak (~13 at%), while its presence in the vacuum-annealed sample spectrum is uncertain. The air-annealed film contains Al^0 residues in the same amount as the corresponding as-reanodized film, while the vacuum-annealed film is Al^0-free. The amount of Al in the surface layer of the PAA-free annealed films is 40–60 at% (when at%(Al + Nb + Mo) = 100%), which is similar to the as-prepared films. The PAA-half-etched air-annealed sample (Fig. S6i†) does not have Al^{3+}–OH coordination, which indicates that the hydroxylated alumina resides in the rods' roots. On the other hand, the Al 2p spectrum of the PAA-inbuilt vacuum-annealed film (Fig. 5c) has an intense peak attributed to the Al^{3+}–OH coordination (18 at%).

Summarizing the XPS analysis results, the surface layers of the nanoarrays prepared in this study comprise stoichiometric MoO_3, molybdenum suboxides (Mo^{5+} and Mo^{4+}), stoichiometric Nb_2O_5, niobium suboxides (Nb^{4+} and Nb^{3+}), and Al_2O_3, distributed as depicted in Fig. 6 and mixed at the molecular level. The inner part of the rods is a slightly reduced pure MoO_3. The overall surface content of Mo increases up to 23 at% with increasing re-anodizing voltage, thinning the Nb interlayer, and annealing the films at 550 °C.

3.1.4. Crystallographic analysis. Fig. S7† shows 2D and extracted conventional as-recorded, calculated, and difference

diffractograms of the OX48-based samples: as-prepared OX48, OX48-180, and OX48-220 samples, vacuum-annealed OX48-220 and air-annealed OX48-220 samples in the 2θ range of 20–90°. The crystal structures for all phases were identified from the ICSD database (FIZ, 2015); the main refinement parameters, details of the XRD line profiles, and the results of quantitative phase analysis are available in the ESI.† For visually estimating the changes in the film's crystal structure with re-anodizing and annealing, the recorded diffractograms are collected in a single plot in Fig. 7.

The diffractograms of all the samples are interpreted with the presence of a polycrystalline metallic Mo phase ($Im\bar{3}m$ space group, crystallite size of 20 to 30 nm), which reveals a preferred orientation growth along ⟨110⟩ direction and is associated with a layer of unoxidized Mo. Since the intensities of the dominating (110) Mo peaks in the diffractograms of the re-anodized, vacuum-annealed, and air-annealed samples are comparable, it is assumed that the thickness of the remaining Mo underlayer is not affected by the 550 °C annealing. This may be explained by the thick anodic oxides above the Mo metal obstructing oxygen diffusion under the chosen annealing conditions.

Another feature is that the anodized OX48 sample contains Al and Nb metals. This agrees with the SEM and XPS results for OX48. From the OX48-180 sample's diffractogram, it is assumed that the Al metal is fully consumed while the residues of the Nb metal network remain on the sample surface. Since (110) Nb peak disappears from the diffractogram of the OX48-220 sample, the Nb metal becomes fully oxidized at U_r > 180 V. The absence of any oxide phases in the as-anodized and re-anodized samples confirms that the electrochemically grown oxides are entirely amorphous.

Contrarily, the annealed OX48-220 films contain well-identified nanocrystalline monoclinic MoO_2 phase ($P2_1/c$ space group, crystallite size ~19 nm) in the amount of 24 wt% in the vacuum-annealed sample and 33 wt% in the air-annealed sample. Additionally, the air-annealed sample contains ~5 wt% orthorhombic Nb_2O_5 nanocrystallites (*Pbam* space group). The MoO_2 nanocrystallites grow with a preferred orientation along $\langle 21\bar{2} \rangle$ direction whereas the Nb_2O_5 nanocrystallites are highly oriented along ⟨001⟩ and ⟨100⟩ directions. The Nb_2O_5 phase is also present in the vacuum-annealed sample in a minor amount, which makes it difficult to estimate the crystallite size reliably.

The more considerable total amount of crystalline oxides in the air-annealed OX48-220 sample relative to the vacuum-annealed sample (~38 *vs.* ~26 wt%) implies that a bigger portion of initially amorphous anodic oxides crystallizes due to the heating in air.

3.1.5. Film formation mechanism. Fig. 8 shows SEM images of selected fragments of cross-fractures of the OX48-180 sample. Due to dissimilar materials in the stack and their mechanical properties, the break divided the sample unevenly, such that several essential features may be visually distinguished, which are not apparent in the images in Fig. 2 and 3. This observation confirms the core/shell structure of the protrusions above the bottom-oxide layer and its graded composition. Combining the SEM, XPS, and XRD interpretation results, visualized preliminary in the schematics of Fig. 6, we propose a model of the nucleation and growth of PAA-assisted MoO_x-based nanostructures (Fig. 9).

According to the model, the sputter-deposited Al/Nb/Mo trilayer on a SiO_2/Si wafer (Fig. 9a) is anodized (Fig. 9b) until the underlying Nb is reached (Fig. 9c). The nucleation and growth of niobium-oxide nanostructures under the pores till the end of stage I is described in detail in our previous publication and may be inherited for the present case.[13] The difference, however, is that the thickness of the Nb interlayer is insufficient to preserve the underlying Mo from anodic oxidation. In other words, molybdenum anodizing starts already during the current decay at stage I, and Mo^{n+} cations begin to migrate outwards

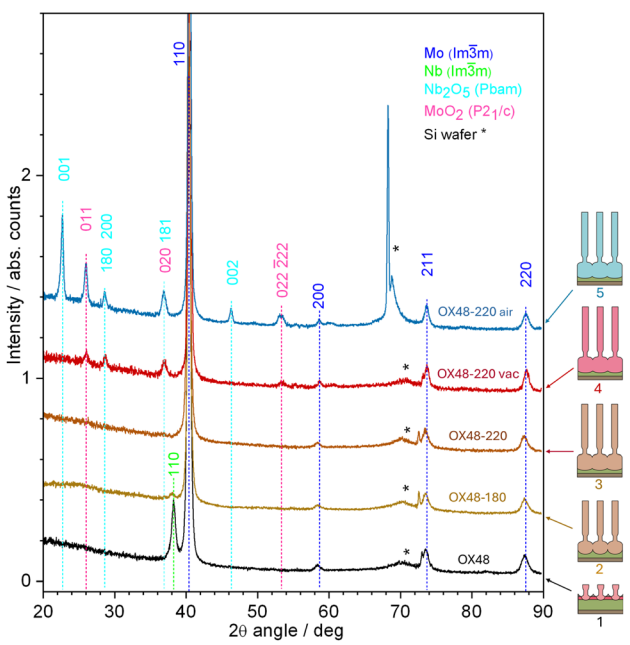

Fig. 7 Comparative X-ray diffractograms for the (1) OX48, (2) OX48-180, (3) OX48-220, (4) vacuum-annealed OX48-220, and (5) air-annealed OX48-220 samples.

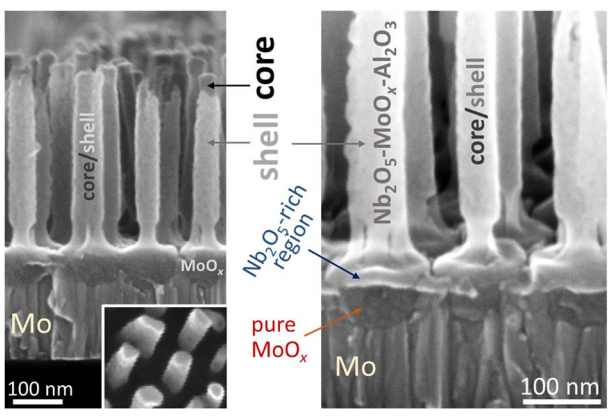

Fig. 8 SEM images of fragments of cross-fractures of the OX48-180 sample disclosing a core/shell heterostructure of the oxide nanorods and uneven composition of the bottom-oxide layer.

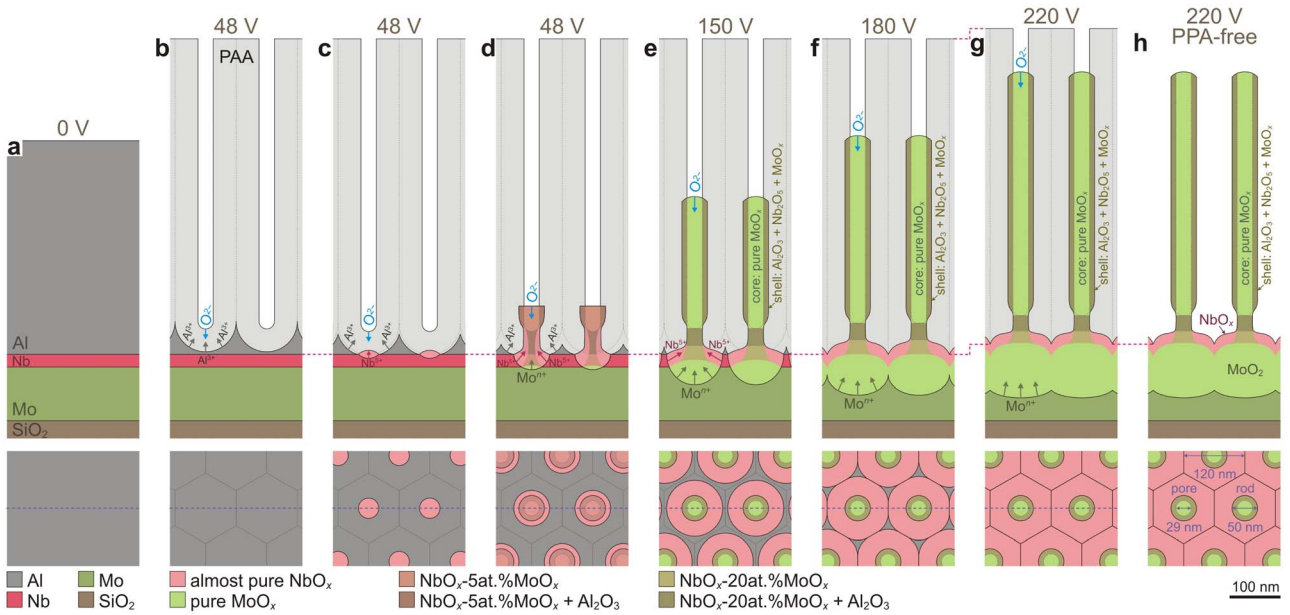

Fig. 9 Schematic model of film growth: (a) the deposition of an Al/Nb/Mo trilayer, (b) the porous anodizing of aluminum in 0.6 M oxalic acid at $U_{st} = 48$ V, (c) the beginning of niobium oxidation, (d) the end of the anodizing stage I as in Fig. 1a, (e) the re-anodizing to 150 V to grow mixed-oxide nanorods, (f and g) the re-anodizing to respectively 180 and 220 V to extend the rods in the pores, (h) the selective PAA dissolution. The lower panel shows the surface fragments corresponding to the upper cross-sections after an imaginary dissolution of the PAA overlayer. The dotted line across the surface fragments shows the position of the imaginary section plane. The colors differentiate the oxides and component concentrations, as the legends show.

once the anodizing front touches the Mo underlayer. Therefore, the nanogoblets in Fig. 9d contain molybdenum oxides mixed with niobium oxides and alumina originating from the PAA barrier layer. The end of stage I features the residues of the Al/Nb bilayer in the form of a continuous network surrounding the goblets. The mechanism for forming such a network is based on the relation between the ionic resistances of the anodic alumina and niobia, as described in detail elsewhere.[13,35]

During the re-anodizing (stage II), the remaining Al/Nb network is gradually consumed, while the Mo layer is further oxidized and the rods grow steadily within the pores. The Al/Nb consumption competes with further molybdenum oxidation until neighboring molybdenum-oxide areas incorporated into the metal expand and merge to form a relatively uniform bottom layer, though having a wavy profile at the MoO_x/Mo interface even at the final re-anodizing voltage of 220 V. The shells of the rods form due to the simultaneous migration of Mo^{n+} ($n = 4$–6) and Nb^{5+} cations in the outer part of the pore walls, which are more defective, less dense, and contaminated by electrolyte-derived species, such as $C_2O_4^{2-}$ in the case of oxalic-acid anodizing.[56] During the upward oxide growth, the alumina partially dissolves from the outmost surface of the pore walls.[57] The degree of such dissolution impacts the amount of alumina that becomes included in the shell composition and remains after the PAA dissolution. Thus, the shells of the rods derived after the PAA dissolution are composed of various molybdenum oxides (Mo^{6+}, Mo^{5+}, Mo^{4+}), stoichiometric Nb_2O_5, and Al_2O_3, all mixed at the molecular level.

In contrast with the shells, the cores are pure molybdenum oxide, which grows without mixing with niobium oxide and does not include alumina because it forms inside the pores without interacting with the pore walls. The absence of niobium oxide in the core composition is explained by the prevalent migration of Nb^{5+} within the shells and by the shortage of niobium supply from the 25 nm thick Nb interlayer (see also the quantitative analysis presented in the ESI† file). Within the core, MoO_3 (dominating amount) is mixed at the molecular level with minor amounts of oxide-hydroxide $MoO_{3-x}(OH)_{2x}$ and molybdenum suboxide Mo_2O_5, which reminds the case of anodizing an Al/W couple.[17,58] The electronic properties of the cores/shells heterostructures will be discussed in Section 3.2.

The thin oxide layer, shown as a pink strip (upper row of Fig. 9) and pink circles (lower row of Fig. 9) covering the deep-laying part of the bottom layer, is a reduced NbO_x (dominating amount) mixed with a minor amount of MoO_2. The innermost anodic oxide composing the semi-balls, balls, and merging balls (Fig. 9) is pure molybdenum suboxide, likely MoO_2, free from niobium-oxide contamination. This is because the oxide within the balls is formed exclusively *via* the migration of O^{2-} (OH^-) from the electrolyte through the NbO_x interlayer, which resides above the Mo layer and has a physically sharp interface.

The last formation step shown in panel (h) is the PAA dissolution. It can be managed selectively toward the nanorods, an excellent achievement of our work. The rods survive the treatment because the multicomponent shell composition prevents the molybdenum anodic oxides from chemical dissolution.

3.1.6. Impact of annealing. Finally, let us consider the effect of annealing. The heating of the PAA-inbuilt OX48-220

sample at 550 °C leads to an amorphous-to-crystalline transition of the MoO_2 and Nb_2O_5 most probably in the bottom oxide only (as visualized in Fig. 6b and c), whereas the rods' cores and shells remain amorphous. This conclusion is based on our experience with the other PAA-assisted metal oxides[48,55,59] and is supported by a calculation using the XRD data (see ESI†). Furthermore, the annealing in ambient air does not cause thermal oxidation of the remaining Mo metal because it is covered with a sufficiently thick layer of nanocomposite metal oxides, which serves as a barrier for oxygen from the air to diffuse through and reach the oxide/molybdenum-metal interface. Along with the amorphous-to-crystalline transition, the oxidation state of molybdenum ions in the Mo–O system increases, which may be explained by oxygen uptake during the interaction of molybdenum suboxides with oxygen in the air:

$$2MoO_2 + O_2 \rightarrow 2MoO_3 \quad (1)$$

$$2Mo_2O_5 + O_2 \rightarrow 4MoO_3 \quad (2)$$

Along with similar crystallization effects, the paradoxical increase in the amount of MoO_3 in the rods' shell of the vacuum-annealed OX48-220 film (Fig. 4j), exceeding that in the air-annealed film (Fig. 4g), may be caused by irreversible heat-enabled diffusion of niobium cations away from Nb_2O_5 in the rods' shells, driven by a concentration gradient in the oxygen-deficient atmosphere (as depicted in Fig. 6c), *i.e.*, at circumstances when oxygen uptake is impossible.[22] Such a prevalent disruption of Nb_2O_5 in the mixed niobium–molybdenum oxides seems reasonable because the bond energy of O–Nb (328 kJ mol^{-1})[60] is lower than that of O–Mo (359 kJ mol^{-1}).[27] The released oxygen anions oxidize the molybdenum suboxide(s), thus increasing the oxidation state of MoO_x in the shells. The released Nb^{5+} cations likely diffuse into the cores, increasing the Mo/Nb ratio in the shells (Fig. 6c). The lowering of Nb (increasing of Mo) amount in the shells due to the vacuum annealing agrees well with the XPS analysis results summarized in Fig. 6c. Such an impact of vacuum annealing is unique since it has not been reported for any nanostructured oxides made *via* the PAA-assisted anodizing of valve metals.[61]

The vacuum annealing does not cause lattice expansion of the Mo metal phase, which means the oxygen species do not diffuse from the oxide into the interstitial sites of the remaining Mo metal.[22] It is thermodynamically possible that the oxide within the nanoballs in the bottom layer reacts with the substrate metal, causing the loss of oxygen from the deep-laying MoO_2.[23] Even if this is also likely kinetically, the effect is too minor to be detected by XRD and has no relation to the oxides composing the cores and the shells.

3.2. Functional properties and potential application

The functional properties of selected nanoarrays prepared here were examined by electrochemical measurements, such as CV, GCD testing, and EIS combined with Mott–Schottky analysis to assess the applicability of the nanomaterials as nanoelectrodes for electrochemical energy-storage microdevices. We were motivated by the reports claiming nanostructured MoO_x-containing surfaces as promising pseudocapacitive materials,[9] despite their instability in aqueous electrolytes.[7] It was further expected that the arrays of 1-D nanoprotrusions developed in our work would be advantageous thanks to their high surface area and vastly directional at the nanoscale electron transport.[62] The PAA-inbuilt OX48-180 sample was chosen as the best-characterized film for this examination.

3.2.1. Energy-storage performance. Fig. 10a shows CV curves recorded in the borate buffer at a scan rate of 50 mV s^{-1} between −1.9 and −0.1 V *vs.* Ag/AgCl. The curves feature two cathodic peaks (C1 and C2) at around −1.4 and −1.0 V *vs.* Ag/AgCl and two anodic peaks (A1 and A2) at −0.8 and −0.4 V *vs.* Ag/AgCl, respectively. The peaks are associated with various insertion and extraction processes of Na^+ cations into and from MoO_3.[3,7,63] Therefore, MoO_3 serves as the negative electrode,[62] with charging during the cathodic potential sweep and discharging during the anodic potential sweep, as marked by the arrows in Fig. 10a. By sweeping to more negative and positive potentials, the operational window of 2.9 V was obtained (with the onset of hydrogen and oxygen evolution found at −2.0 and +0.9 V *vs.* Ag/AgCl, respectively, see Fig. S10†), which is broader than reported elsewhere (2.2 and ∼1.5 V).[7,62] This result confirms the suitability of the electrode for electrochemical energy storage and justifies the selected potential window for further analysis. This finding also reveals that the tested sample had poor electroactivity towards water electrolysis, which is

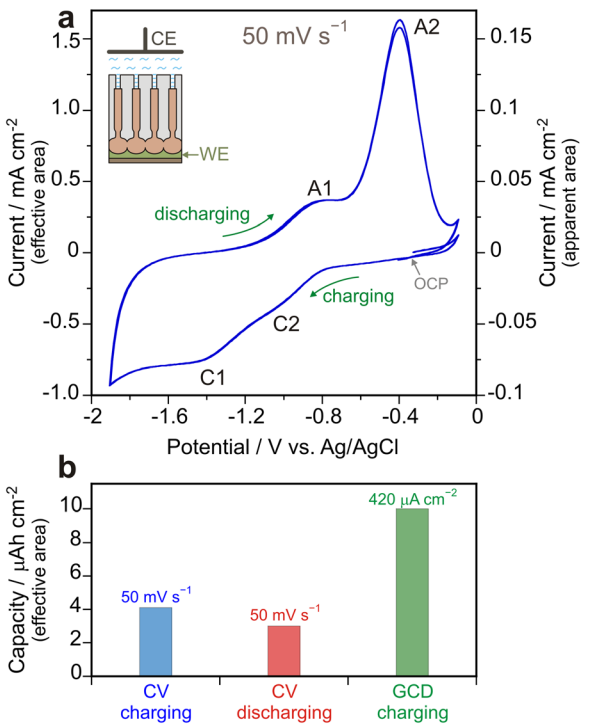

Fig. 10 (a) CV curves (scan rate 50 mV s^{-1}) in the borate buffer solution for the PAA-inbuilt OX48-180 sample. (b) Capacity values calculated from the CV curves and from a comparable galvanostatic charge–discharge (GCD) curve (shown in Fig. S12†), having similar charging times of 36 and 60 s, respectively; the potential range was −0.1 to −1.9 V *vs.* Ag/AgCl. The quantities were related to the apparent (A_a) and effective (A_e) surface areas; $A_e = 0.1 \times A_a$.

advantageous for energy-storage applications. Further, the CV signature of the OX48-180 film seems less typical for pseudocapacitive electrodes and more fitting the battery-like materials, with faradaic-dominated and diffusion-limited current, since the 'mirror-image' criterion is not fulfilled.[64–66]

The level of CV current density (~0.1 mA cm^{-2}, Fig. 10a, right *y*-axis), compared with the literature reports (~10 mA cm^{-2} at 50 mV s^{-1}),[7,62] seems low. On the other hand, in the PAA-inbuilt sample, only about 10% of the apparent surface area (A_a) interacts with the electrolyte, as shown in the embedded schematics in Fig. 10a. Therefore, to judge the actual performance of the material, we relate the CV current density to the effective surface area (A_e), left *y*-axis in Fig. 10a, *i.e.*, as if the measured surface would be a flat MoO_x, then it would reach 1 mA cm^{-2}. Furthermore, using A_e, we calculate the areal capacities from the CV curves (Fig. 10b, the calculations are available in the ESI, Fig. S11†), and the charging capacity of 4.1 μA h cm^{-2} is obtained, which is higher than the discharging capacity (3.1 μA h cm^{-2}), and lower than a charging capacity obtained from the GCD curves (10.2 μA h cm^{-2}, see ESI† for the GCD measurements and corresponding calculations, Fig. S12†). Still, the current densities and discharging capacities of MoO_3 reported for similar potential ranges and discharging times (~10 mA cm^{-2} and ~100 μA h cm^{-2}, respectively)[7,62] are ten-fold higher. The difference is explained by the electrodes' specific structuring rather than the reported materials' superior behavior.[7,62] If the entire surface of the PAA-free OX48-180 sample were involved in the analysis, it would exhibit enhanced characteristics and be highly competitive for the desired application.

3.2.2. Charge-storage mechanisms. The GCD curves of the PAA-inbuilt OX48-180 film (Fig. S12†) reveal a nonlinear shape without apparent potential plateau(s), indicating pseudocapacitive behavior.[64,66,67] Thus, the pseudocapacitive and diffusion-limited mechanisms may occur in the material at the same time. CV measurements were performed at various scan rates to deepen the knowledge of processes during the charging/discharging (Fig. 11a, A_e-value is used here), starting with 250 mV s^{-1} and continuing with consecutively decreasing rates. Again, two anodic peaks (A1 and A2) are observed. However, at the higher scan rates, the two cathodic peaks (inset in Fig. 11a) merge into a single peak (C1). The A1 : A2 ratio of the peak heights lowers with decreasing sweep rate from 0.83 to 0.09, which implies different origins of these peaks. The peak positions are plotted against the scan rate in Fig. 11b. Generally, a shift towards more positive or negative potentials is expected for anodic or cathodic peaks, respectively, in the case of diffusion-limited redox processes (battery-like), whereas a minor shift is associated with the capacitive-like redox or intercalation processes (pseudocapacitive).[7,64,68] A substantial shift is noted here for A2 and C1, whereas A1 keeps its position. Furthermore, the peak current, I_p, is plotted against the scan rate, ν, in a log–log representation (Fig. 11c) to reveal the value for b constant in the expression $I_p = a\nu^b$: $b = 0.5$ means diffusion-controlled charge transport, $b = 1$ capacitive-like behavior, and $0.5 < b < 1$ indicates a mixed control of the processes.[7,64,67] Thus, from Fig. 11c, the A2 peak originates from a diffusion-controlled process, the A1 peak is capacitive-like, and the C1 is under mixed control. These observations agree with the considerations of the peak positions (Fig. 11b). Therefore, *the electrode tested here combines battery-like and capacitor-like behaviors*.

Further, Dunn's approach[7,64] was adopted to deconvolute CV current into diffusive and capacitive current contributions:

$$i(V, \nu) = k_1(V)\nu + k_2(V)\nu^{1/2} \quad (3)$$

which can be rearranged to

$$i(V, \nu)/\nu^{1/2} = k_1(V)\nu^{1/2} + k_2(V) \quad (4)$$

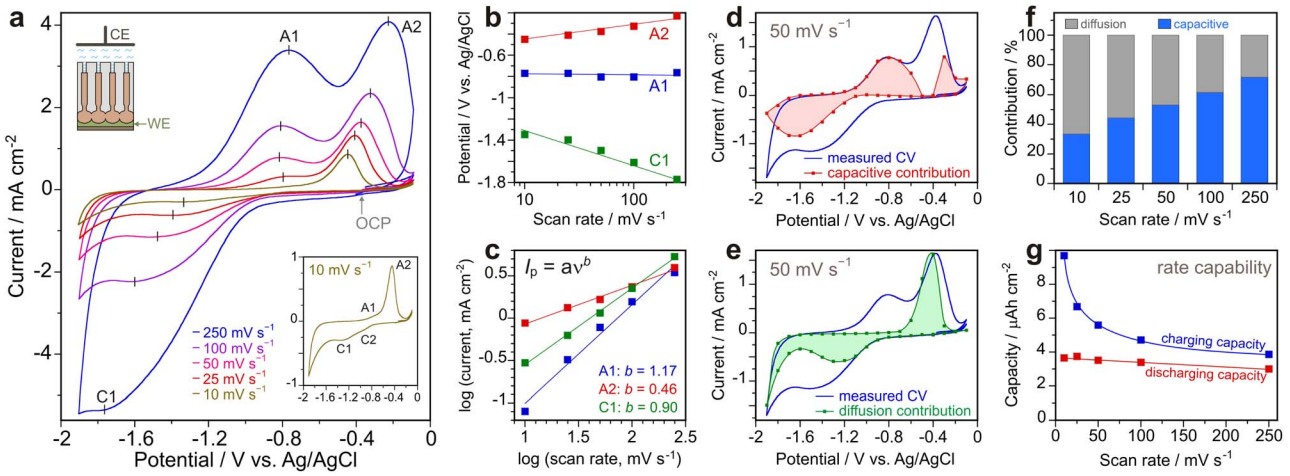

Fig. 11 Scan-rate dependent CV measurements in the borate buffer solution with the PAA-inbuilt OX48-180 sample: (a) experimental CV curves at various scan rates and (b–g) their evaluation. (b) Peak position *vs.* scan rate. (c) Peak height *vs.* scan rate in a log–log plot to obtain *b*-value. (d and e) Experimental (lines) and calculated (lines + symbols) CV curves at 50 mV s^{-1} distinguishing the (d) capacitive and (e) diffusive contributions. (f) Contribution of the diffusion-controlled and capacitive processes of Na^+ insertion *vs.* scan rate. (g) Charging and discharging capacities *vs.* scan rate to determine the electrode's rate capability. All quantities are related to A_e.

where $i(V, \nu)$ is the total current at a particular potential and scan rate, $k_1(V)\nu$ is the capacitive current contribution, and $k_2(V)\nu^{1/2}$ is the diffusive current contribution. By plotting $i(V, \nu)/\nu^{1/2}$ *vs.* $\nu^{1/2}$, the potential dependent constants $k_1(V)$ and $k_2(V)$ are obtained (we calculate them with a potential step of 0.1 V). The capacitive and diffusive contributions to the CVs are calculated and plotted for each scan rate; the selected results (for 50 mV s^{-1}) are presented in Fig. 11d and e. Pairs of broad capacitive redox peaks (at −1.65 and −0.8 V *vs.* Ag/AgCl) and relatively narrower diffusive redox peaks (at −1.25 and −0.45 V *vs.* Ag/AgCl) are noted, likely originating from the Na^+ cation insertion and extraction and corresponding to the C1/A1 and C2/A2 redox couples. The capacitive pair is assumed to reflect a near-surface redox/intercalation reaction, whereas the diffusive pair belongs to a deeper redox/intercalation reaction, which can formally be written as:[63]

Charging:

$$Mo^{VI}O_3 + Na^+ + e^- \rightarrow NaMo^{V}O_3 \quad (5)$$

$$Mo_2^{V}O_5 + Na^+ + e^- \rightarrow NaMo^{IV}Mo^{V}O_5 \quad (6)$$

Discharging:

$$NaMo^{V}O_3 \rightarrow Mo^{VI}O_3 + Na^+ + e^- \quad (7)$$

$$NaMo^{IV}Mo^{V}O_5 \rightarrow Mo_2^{V}O_5 + Na^+ + e^- \quad (8)$$

This CV deconvolution analysis eventually confirms that the A1, A2, and C1 peaks are due to the capacitive, diffusive, and mixed contributions, respectively.

An extra contribution to the diffusive current at potentials below −1.8 V *vs.* Ag/AgCl (Fig. 11e) is attributed to the hydrogen evolution reaction. It occurs at less negative potentials than initially assumed (*i.e.*, beyond −2.0 V *vs.* Ag/AgCl; see Fig. S10†). The extra 'peak' in the capacitive current at −0.3 V *vs.* Ag/AgCl (Fig. 9d) is likely an artifact of the deconvolution since this approach does not consider the peak shift effect with increasing sweep rate.[64] Finally, the ratios of capacitive and diffusive contributions to the CV curves are calculated for each scan rate (Fig. 11f). The capacitive current dominates at the higher scan rates, while the diffusive contribution is more significant at the lower scan rates.

The scan-rate-dependent CVs (Fig. 11a) are used to calculate the specific *charging* and *discharging capacities* and to estimate the *rate capability* of the OX48-180 film (Fig. 11g). The difference between the charging and discharging capacities, especially at the low scan rates, is attributed to a substantial negative current due to the hydrogen evolution during the cathodic and anodic sweeps, which lowers the efficiency of the electrode in the investigated potential window. Therefore, a narrower window is needed for practical use, limited by −1.6 V *vs.* Ag/AgCl. An insignificant decrease in discharging capacity from ~4 to 3 μA h cm^{-2} with increasing scan rate implies an excellent rate capability of the electrode.[7,67]

3.2.3. Film semiconducting properties. The capacitive contribution of a MoO_3 electrode can reportedly be enhanced by introducing oxygen vacancies in the oxide,[63] which act as electron donors in MoO_3 n-type semiconductors.[3] We estimated the donor concentration, N_d, for the OX48-180 PAA-inbuilt sample by Mott–Schottky analysis of the EIS data acquired at various potentials;[17,69,70] the details are shown in Fig. S13.† Although various contributions to the total impedance beside the depletion layer complicate the analysis of battery-like and pseudocapacitive materials,[71] we could estimate $N_d = 1 \times 10^{22}$ cm^{-3} (the details are described in the ESI†). The value implies a highly doped n-type semiconductor,[70] which means the difficulty in further increasing the capacitive contribution by introducing more oxygen vacancies. Moreover, the Mott–Schottky analysis reveals a transition from a depletion layer at the MoO_3 rod tops to a conducting oxide around −1.0 V *vs.* Ag/AgCl when measuring from anodic to cathodic potentials (Fig. S13†). Such a transition allows for effective Na^+ intercalation and correlates with increased current density during the cathodic sweeps (Fig. 11a).

3.2.4. Challenges and outlook. The electrochemical experiments demonstrated the high relevance level of the tested electrode for potential energy-storage applications even when such a small fraction as the effective surface area (rods' cores) was involved in the measurements. Should the entire film surface be exposed to the electrolyte, an 8-fold rise in current density and capacity may be expected for the 220 V re-anodized PAA-free film, which would compete with the best-reported values.[7,62,72] However, the CV and Mott–Schottky measurements performed with the OX48-180 *PAA-free* sample (not shown) did not reveal the expected advances, likely because the current flows merely along the amorphous MoO_x nanocores connected to the crystalline MoO_2 bottom layer, while the alumina-containing shells and the bottom oxide's surface are less doped semiconductors or dielectrics (Fig. 6a). This finding differs from our previous works, for instance, on the WO_x- and HfO_x-based nanorod arrays, where the entire rods' surface exhibited excellent electron conductivity.[70,73]

Future work is required to thin the shells and increase their electron conductivity. This might be achieved by playing with anodization variables, applying post-anodizing surface-finishing techniques such as partial wet or plasma chemical fine polishing, doping the shells with electron-conducting elements or compounds, or nitridation techniques.[74] Alternatively, the as-prepared nanoarrays seem highly appropriate without additional treatments as building blocks for nanostructured field-emission, memristive, superconducting, magnetic, or optical nanodevices – where the heterogeneous core/shell nanostructure may be highly advantageous.[13,58,74] These will be the subjects of future research.

4. Conclusions

The following conclusions may be drawn from the present study.

(1) For the first time, arrays of MoO_x-based nanostructures of various sizes and morphologies, vertically aligned on a substrate, have been synthesized self-organized *via* the PAA-assisted anodization of a Mo layer through a very thin Nb interlayer. Such a smart anodization enabled the nucleation

and sustainable growth of fully amorphous MoO_x nanostructures within and under the PAA nanopores, which is impossible by direct molybdenum anodizing or other methods.

(2) The oxide growth occurred *via* the unique outward migration of Mo^{n+} and Nb^{5+} ions through the thin Nb_2O_5 interlayer, alumina barrier layer, along the pore walls, and inside the pores together with the inward migration of O^{2-} (OH^-) ions. Such a cooperative ion transport resulted in a self-organized core/shell architecture of the oxide protrusions: the shells comprise MoO_3, molybdenum suboxides (Mo^{5+} and Mo^{4+}), Nb_2O_5, and Al_2O_3 mixed at the molecular level, whereas the cores are partially hydrated and slightly reduced pure MoO_3. The 550 °C annealing in ambient air or a vacuum (10^{-5} Pa) results in an amorphous-to-crystalline transition in the bottom-oxide layers and partial oxidation of the suboxides in the shells.

(3) The cores of the oxide nanorods exhibit electron transport properties of a highly-doped n-type semiconductor, with N_d reaching 1×10^{22} cm^{-3}, while the shells are less doped semiconductors or dielectrics.

(4) The MoO_x-based nanoarrays revealed the potential for applications in semiconductor nanoelectronics where the intensive and localized at the nanoscale electron transport, reversible redox reactions, high population density of nanochannels (up to 3×10^{10} cm^{-2}), and tailored crystallinity are in demand. The disclosed intercalation pseudocapacitance behavior of the rods' cores and the competitive performance metrics make the films promising as nanostructured electrodes for on-chip energy-related applications. The works to improve the electron-transport properties of the shells, explore field-emission and memristive potentials of the nanoarrays, and design relevant device configurations are in progress and will be reported in due course.

Data availability

The data supporting this article have been included as part of the ESI.†

Author contributions

Alexander Mozalev: conceptualization, methodology, investigation, visualization, writing – review and editing, resources, project administration, and funding acquisition; Maria Bendova: investigation, formal analysis, visualization, validation, and writing – original draft; Lukas Kalina: investigation, data curation; Jan Prasek: investigation; Francesc Gispert-Guirado: investigation, validation, visualization; Eduard Llobet: writing – review and editing, resources, funding acquisition.

Conflicts of interest

There are no conflicts to declare.

Acknowledgements

This research was financially supported by the Czech Science Foundation (GACR), project no. 23-07848S. The CzechNanoLab project LM2023051 funded by the MEYS CR is acknowledged for sputter-deposition and XPS sample analysis at CEITEC Nano Research Infrastructure. We thank then-PhD student Kirill Kamnev for the technical assistance in SEM and XPS recording. E. L. was supported by the Catalan Institution for Research and Advanced Studies *via* the 2023 Edition of the ICREA Academia Award, Catalonia, Spain.

Notes and references

1 I. A. de Castro, R. S. Datta, J. Z. Ou, A. Castellanos-Gomez, S. Sriram, T. Daeneke and K. Kalantar-zadeh, Molybdenum oxides – From fundamentals to functionality, *Adv. Mater.*, 2017, **29**, 1701619, DOI: **10.1002/adma.201701619**.

2 K. Hermann and M. Witko, Chapter 4 – Theory of physical and chemical behavior of transition metal oxides: vanadium and molybdenum oxides, in *Oxide Surfaces*, ed. D. P. Woodruff, Elsevier Science B.V., 2001, pp. 136–198, DOI: **10.1016/S1571-0785(01)80024-9**.

3 C. V. Ramana, A. Mauger and C. M. Julien, Growth, characterization and performance of bulk and nanoengineered molybdenum oxides for electrochemical energy storage and conversion, *Prog. Cryst. Growth Charact. Mater.*, 2021, **67**, 100533, DOI: **10.1016/j.pcrysgrow.2021.100533**.

4 T. R. Lenka and H. P. T. Nguyen, *Nanoelectronic Devices and Applications*, Bentham Science Publishers, 2024, DOI: **10.2174/9789815238242124010101**.

5 R. Malik, N. Joshi and V. K. Tomer, Advances in the designs and mechanisms of MoO_3 nanostructures for gas sensors: a holistic review, *Materials Advances*, 2021, **2**, 4190–4227, DOI: **10.1039/D1MA00374G**.

6 Y. Jiang, Y. Wang, J. Ni and L. Li, Molybdenum-based materials for sodium-ion batteries, *InfoMat*, 2021, **3**, 339–352, DOI: **10.1002/inf2.12175**.

7 A. E. Elkholy, T. T. Duignan, X. Sun and X. Song Zhao, Stable α-MoO_3 electrode with a widened electrochemical potential window for aqueous electrochemical capacitors, *ACS Appl. Energy Mater.*, 2021, **4**, 3210–3220, DOI: **10.1021/acsaem.0c02990**.

8 H. Wang, T. Li, A. M. Hashem, A. E. Abdel-Ghany, R. S. El-Tawil, H. M. Abuzeid, A. Coughlin, K. Chang, S. Zhang, H. El-Mounayri, A. Tovar, L. Zhu and C. M. Julien, Nanostructured molybdenum-oxide anodes for lithium-ion batteries: an outstanding increase in capacity, *Nanomaterials*, 2021, **12**, 13, DOI: **10.3390/nano12010013**.

9 B. Hu, L. Mai, W. Chen and F. Yang, From MoO_3 nanobelts to MoO_2 nanorods: structure transformation and electrical transport, *ACS Nano*, 2009, **3**, 478–482, DOI: **10.1021/nn800844h**.

10 Y. Jia and Y. Ma, Advances in MoO_3-based supercapacitors for electrochemical energy storage, *J. Energy Storage*, 2024, **85**, 111103, DOI: **10.1016/j.est.2024.111103**.

11 A. A. Shaikh, J. Bhattacharjee, P. Datta and S. Roy, A comprehensive review of the oxidation states of molybdenum oxides and their diverse applications,

Sustainable Chemistry for the Environment, 2024, **7**, 100125, DOI: 10.1016/j.scenv.2024.100125.

12 P. Bhol, M. B. Bhavya, S. Swain, M. Saxena and A. K. Samal, Miniaturization on chip nano energy application, in *Nanotechnology in Miniaturization, an Emerging Trend to Fabricate Future Devices*, ed. S. K. Shukla, C. M. Hussain, B. Mangla, M. Choudhary and S. Patra, Springer, 2024, pp. 173–196.

13 A. Mozalev, R. M. Vázquez, C. Bittencourt, D. Cossement, F. Gispert-Guirado, E. Llobet and H. Habazaki, Formation–structure–properties of niobium-oxide nanocolumn arrays via self-organized anodization of sputter-deposited aluminum-on-niobium layers, *J. Mater. Chem. C*, 2014, **2**, 4847–4860, DOI: 10.1039/c4tc00349g.

14 C. Fernández-González, S. Ruiz-Gómez, A. Arché-Núñez, L. Pérez and C. Tavares de Sousa, Nano-patterning using ultra-thin alumina membranes, *Mater. Today Nano*, 2025, **29**, 100553, DOI: 10.1016/j.mtnano.2024.100553.

15 N. I. Tatarenko and A. M. Mozalev, Geometry and element composition of a nanoscale field emission array formed by self-organization in porous anodic aluminum oxide, *Solid-State Electron.*, 2001, **45**, 1009–1016, DOI: 10.1016/S0038-1101(01)00022-3.

16 A. Mozalev, M. Sakairi, I. Saeki and H. Takahashi, Nucleation and growth of the nanostructured anodic oxides on tantalum and niobium under the porous alumina film, *Electrochim. Acta*, 2003, **48**, 3155–3170, DOI: 10.1016/S0013-4686(03)00345-1.

17 A. Mozalev, M. Bendova, F. Gispert-Guirado, Z. Pytlicek and E. Llobet, Metal-substrate-supported tungsten-oxide nanoarrays via porous-alumina-assisted anodization: from nanocolumns to nanocapsules and nanotubes, *J. Mater. Chem. A*, 2016, **4**, 8219–8232, DOI: 10.1039/C6TA02027E.

18 S. H. Park, Y. H. Kim, T. G. Lee, H. K. Shon, H. M. Park and J. Y. Song, Synthesis and electrochemical capacitance of long tungsten oxide nanorod arrays grown vertically on substrate, *Mater. Res. Bull.*, 2012, **47**, 3612–3618, DOI: 10.1016/j.materresbull.2012.06.053.

19 A. Mozalev, M. Bendova, F. Gispert-Guirado and E. Llobet, Hafnium-oxide 3-D nanofilms via the anodizing of Al/Hf metal layers, *Chem. Mater.*, 2018, **30**, 2694–2708, DOI: 10.1021/acs.chemmater.8b00188.

20 S. Z. Chu, K. Wada, S. Inoue and H. Segawa, Direct growth of highly ordered crystalline zirconia nanowire arrays with high aspect ratios on glass by a tailored anodization, *J. Electrochem. Soc.*, 2011, **157**, C148–C157, DOI: 10.1149/1.3568997.

21 A. Mozalev, Z. Pytlicek, K. Kamnev, J. Prasek, F. Gispert-Guirado and E. Llobet, Zirconium oxide nanoarrays via the self-organized anodizing of Al/Zr bilayers on substrates, *Mater. Chem. Front.*, 2021, **5**, 1917–1931, DOI: 10.1039/D0QM00862A.

22 B. Jin, X. Zhou, L. Huang, M. Lickleder, M. Yang and P. Schmuki, Aligned MoO_x/MoS_2 core–shell nanotubular structures with a high density of reactive sites based on self-ordered anodic molybdenum oxide nanotubes, *Angew. Chem., Int. Ed.*, 2016, **55**, 12252–12256, DOI: 10.1002/anie.201605551.

23 M. R. Arora and R. Kelly, The structure and stoichiometry of anodic films on V, Nb, Ta, Mo and W, *J. Mater. Sci.*, 1977, **12**, 1673–1684, DOI: 10.1007/BF00542819.

24 Ø. S. Fjellvåg, A. Ruud, H. H. Sønsteby, O. Nilsen and H. Fjellvåg, Crystallization, phase stability, and electrochemical performance of β-MoO_3 thin films, *Cryst. Growth Des.*, 2020, **20**, 3861–3866, DOI: 10.1021/acs.cgd.0c00156.

25 M. Bojinov, I. Betova and R. Raicheff, Transpassivity of molybdenum in H_2SO_4 solution, *J. Electroanal. Chem.*, 1995, **381**, 123–131, DOI: 10.1016/0022-0728(94)03675-S.

26 W. A. Badawy and F. M. Al-Kharafi, Corrosion and passivation behaviors of molybdenum in aqueous solutions of different pH, *Electrochim. Acta*, 1998, **44**, 693–702, DOI: 10.1016/S0013-4686(98)00180-7.

27 H. Habazaki, M. Uozumi, H. Konno, K. Shimizu, S. Nagata, K. Asami, P. Skeldon and G. E. Thompson, Influence of molybdenum species on growth of anodic titania, *Electrochim. Acta*, 2002, **47**, 3837–3845, DOI: 10.1016/S0013-4686(02)00319-5.

28 V. S. Saji and C.-W. Lee, Molybdenum, molybdenum oxides, and their electrochemistry, *ChemSusChem*, 2012, **5**, 1146–1161, DOI: 10.1002/cssc.201100660.

29 H. Habazaki, M. Uozumi, H. Konno, S. Nagata and K. Shimizu, Formation of barrier-type amorphous anodic films on Ti–Mo alloys, *Surf. Coat. Technol.*, 2003, **169–170**, 151–154, DOI: 10.1016/S0257-8972(03)00216-0.

30 A. Mozalev and J. Hubalek, On-substrate porous-anodic-alumina-assisted gold nanostructure arrays: Meeting the challenges of various sizes and interfaces, *Electrochim. Acta*, 2019, **297**, 988–999, DOI: 10.1016/j.electacta.2018.11.192.

31 S. Ono, M. Saito and H. Asoh, Self-ordering of anodic porous alumina formed in organic acid electrolytes, *Electrochim. Acta*, 2005, **51**, 827–833, DOI: 10.1016/j.electacta.2005.05.058.

32 C. S. Blackman, X. Correig, V. Katko, A. Mozalev, I. P. Parkin, R. Alcubilla and T. Trifonov, Templated growth of tungsten oxide micro/nanostructures using aerosol assisted chemical vapour deposition, *Mater. Lett.*, 2008, **62**, 4582–4584, DOI: 10.1016/j.matlet.2008.08.027.

33 T. Kikuchi, A. Takenaga, S. Natsui and R. O. Suzuki, Advanced hard anodic alumina coatings via etidronic acid anodizing, *Surf. Coat. Technol.*, 2017, **326**, 72–78, DOI: 10.1016/j.surfcoat.2017.07.043.

34 V. Surganov, P. Morgen, J. G. Nielsen, G. Gorokh and A. Mozalev, Study of the initial stage of aluminium anodization in malonic acid solution, *Electrochim. Acta*, 1987, **32**, 1125–1127, DOI: 10.1016/0013-4686(87)90043-0.

35 K. Kamnev, M. Bendova, Z. Fohlerova, T. Fialova, O. Martyniuk, J. Prasek, K. Cihalova and A. Mozalev, Arrays of ultra-thin selenium-doped zirconium-anodic-oxide nanorods as potential antibacterial coatings, *Mater. Chem. Front.*, 2025, **9**, 866–883, DOI: 10.1039/D4QM01081G.

36 A. Mozalev, M. Bendova, F. Gispert-Guirado, E. Llobet and H. Habazaki, Porous-anodic-alumina-templated Ta-Nb-alloy/oxide coatings via the magnetron-sputtering/anodizing as novel 3D nanostructured electrodes for energy-storage applications, *Surf. Coat. Technol.*, 2024, **489**, 131042, DOI: 10.1016/j.surfcoat.2024.131042.

37 B. P. Payne, M. C. Biesinger and N. S. McIntyre, X-ray photoelectron spectroscopy studies of reactions on chromium metal and chromium oxide surfaces, *J. Electron Spectrosc. Relat. Phenom.*, 2011, **184**, 29–37, DOI: 10.1016/j.elspec.2010.12.001.

38 G. Ning and R. L. Flemming, Rietveld refinement of LaB_6: Data from μXRD, *J. Appl. Crystallogr.*, 2005, **38**, 757–759, DOI: 10.1107/S0021889805023344.

39 H. M. Rietveld, A profile refinement method for nuclear and magnetic structures, *J. Appl. Crystallogr.*, 1969, **2**, 65–71, DOI: 10.1107/S0021889869006558.

40 A. A. Coelho, TOPAS and TOPAS-Academic: An optimization program integrating computer algebra and crystallographic objects written in C++, *J. Appl. Crystallogr.*, 2018, **51**, 210–218, DOI: 10.1107/S1600576718000183.

41 A. Mozalev, S. Magaino and H. Imai, The formation of nanoporous membranes from anodically oxidized aluminium and their application to Li rechargeable batteries, *Electrochim. Acta*, 2001, **46**, 2825–2834, DOI: 10.1016/S0013-4686(01)00497-2.

42 L. Zaraska, M. Jaskuła and G. Sulka, Porous anodic alumina layers with modulated pore diameters formed by sequential anodizing in different electrolytes, *Mater. Lett.*, 2016, **171**, 315–318, DOI: 10.1016/j.matlet.2016.02.113.

43 K. S. Napolskii, I. V. Roslyakov, A. A. Eliseev, D. V. Byelov, A. V. Petukhov, N. A. Grigoryeva, W. G. Bouwman, A. V. Lukashin, A. P. Chumakov and S. V. Grigoriev, The kinetics and mechanism of long-range pore ordering in anodic films on aluminum, *J. Phys. Chem. C*, 2011, **115**, 23726–23731, DOI: 10.1021/jp207753v.

44 A. Jagminas and I. Vrublevsky, Chapter three - Anodizing of aluminum under the burning conditions, in *Nanostructured Anodic Metal Oxides*, ed. G. D. Sulka, Elsevier, 2020, pp. 89–122, DOI: 10.1016/B978-0-12-816706-9.00003-0.

45 J. P. S. Pringle, The anodic oxidation of superimposed metallic layers: theory, *Electrochim. Acta*, 1980, **25**, 1423–1437, DOI: 10.1016/0013-4686(80)87157-X.

46 M. G. Blamire, K. H. Huang, R. E. Somekh, E. C. G. Kirk, G. W. Morris and J. E. Evetts, Direct observation of atomic planes in epitaxial multilayers by anodization spectroscopy, *Appl. Phys. Lett.*, 1989, **55**, 732–734, DOI: 10.1063/1.101789.

47 O. V. Kupreeva, D. A. Tsirkunov, G. G. Rabatuev, S. K. Lazarouk, X. Huang, W. Su, L. Sun, J. Liu and D. A. Sasinovich, Effect of anodic voltage on parameters of porous alumina formed in sulfuric acid electrolytes, *Mater. Phys. Mech.*, 2019, **41**, 62–68, DOI: 10.18720/MPM.4112019_9.

48 K. Kamnev, M. Sepúlveda, M. Bendova, Z. Pytlicek, J. Prasek, E. Kolibalova, J. Michalicka and A. Mozalev, The growth, composition, and functional properties of self-organized nanostructured ZrO_2-Al_2O_3 anodic films for advanced dielectric applications, *Adv. Electron. Mater.*, 2021, **7**, 2100505, DOI: 10.1002/aelm.202100505.

49 K. Kamnev, M. Bendova, Z. Pytlicek, J. Prasek, L. Kejík, F. Güell, E. Llobet and A. Mozalev, Se-doped Nb_2O_5–Al_2O_3 composite-ceramic nanoarrays via the anodizing of Al/Nb bilayer in selenic acid, *Ceram. Int.*, 2023, **49**, 34712–34725, DOI: 10.1016/j.ceramint.2023.08.134.

50 G. Knörnschild, A. A. Poznyak, A. G. Karoza and A. Mozalev, Effect of the anodization conditions on the growth and volume expansion of porous alumina films in malonic acid electrolyte, *Surf. Coat. Technol.*, 2015, **275**, 17–25, DOI: 10.1016/j.surfcoat.2015.04.030.

51 P. A. Spevack and N. S. McIntyre, Thermal reduction of MoO_3, *J. Phys. Chem.*, 1992, **96**, 9029–9035, DOI: 10.1021/j100201a062.

52 D. O. Scanlon, G. W. Watson, D. J. Payne, G. R. Atkinson, R. G. Egdell and D. S. L. Law, Theoretical and experimental study of the electronic structures of MoO_3 and MoO_2, *J. Phys. Chem. C*, 2010, **114**, 4636–4645, DOI: 10.1021/jp9093172.

53 I. A. Okonkwo, J. Doff, A. Baron-Wiechec, G. Jones, E. V. Koroleva, P. Skeldon and G. E. Thompson, Oxidation states of molybdenum in oxide films formed in sulphuric acid and sodium hydroxide, *Thin Solid Films*, 2012, **520**, 6318–6327, DOI: 10.1016/j.tsf.2012.05.031.

54 B. R. Strohmeier, An ESCA method for determining the oxide thickness on aluminum alloys, *Surf. Interface Anal.*, 1990, **15**, 51–56, DOI: 10.1002/sia.740150109.

55 M. Bendova, J. Kolar, M. Marik, T. Lednicky and A. Mozalev, Influence of nitrogen species on the porous-alumina-assisted growth of TiO_2 nanocolumn arrays, *Electrochim. Acta*, 2018, **281**, 796–809, DOI: 10.1016/j.electacta.2018.05.197.

56 I. Vrublevsky, V. Parkoun, V. Sokol and J. Schreckenbach, Study of chemical dissolution of the barrier oxide layer of porous alumina films formed in oxalic acid using a re-anodizing technique, *Appl. Surf. Sci.*, 2004, **236**, 270–277, DOI: 10.1016/j.apsusc.2004.04.030.

57 A. Mozalev, A. J. Smith, S. Borodin, A. Plihauka, A. W. Hassel, M. Sakairi and H. Takahashi, Growth of multioxide planar film with the nanoscale inner structure via anodizing Al/Ta layers on Si, *Electrochim. Acta*, 2009, **54**, 935–945, DOI: 10.1016/j.electacta.2008.08.030.

58 M. Bendova, J. Hubalek and A. Mozalev, Exploring electron transport and memristive switching in nanoscale Au/WO_x/W multijunctions based on anodically oxidized Al/W metal layers, *Adv. Mater. Interfaces*, 2016, **3**, 1600512, DOI: 10.1002/admi.201600512.

59 M. Bendova, J. Kolar, F. Gispert-Guirado and A. Mozalev, Porous-alumina-assisted growth of nanostructured anodic films on Ti–Nb alloys, *ChemElectroChem*, 2018, **5**, 2825–2835, DOI: 10.1002/celc.201800785.

60 H. Habazaki, T. Matsuo, H. Konno, K. Shimizu, S. Nagata, K. Matsumoto, K. Takayama, Y. Oda, P. Skeldon and G. E. Thompson, Influence of silicon species on the

electric properties of anodic niobia, *Electrochim. Acta*, 2003, **48**, 3519–3526, DOI: 10.1016/S0013-4686(03)00473-0.

61 A. Mozalev, V. Khatko, C. Bittencourt, A. W. Hassel, G. Gorokh, E. Llobet and X. Correig, Nanostructured columnlike tungsten oxide film by anodizing Al/W/Ti layers on Si, *Chem. Mater.*, 2008, **20**, 6482–6493, DOI: 10.1021/cm801481z.

62 B. Jin, S. Hejazi, F. Pyczak, M. Oehring, S. Mohajernia, S. Kment, O. Tomanec, R. Zboril, N. T. Nguyen, M. Yang and P. Schmuki, Amorphous Mo–Ta oxide nanotubes for long-term stable Mo oxide-based supercapacitors, *ACS Appl. Mater. Interfaces*, 2019, **11**, 45665–45673, DOI: 10.1021/acsami.9b15958.

63 H.-S. Kim, J. B. Cook, H. Lin, J. S. Ko, S. H. Tolbert, V. Ozolins and B. Dunn, Oxygen vacancies enhance pseudocapacitive charge storage properties of MoO_{3-x}, *Nat. Mater.*, 2017, **16**, 454–460, DOI: 10.1038/nmat4810.

64 S. Fleischmann, J. B. Mitchell, R. Wang, C. Zhang, D. Jiang, V. Presser and V. Augustyn, Pseudocapacitance: From fundamental understanding to high power energy storage materials, *Chem. Rev.*, 2020, **120**, 6738–6782, DOI: 10.1021/acs.chemrev.0c00170.

65 T. Brousse, D. Bélanger and J. W. Long, To Be or Not To Be Pseudocapacitive?, *J. Electrochem. Soc.*, 2015, **162**, A5185–A5189, DOI: 10.1149/2.0201505jes.

66 Y. Gogotsi and R. M. Penner, Energy storage in nanomaterials – capacitive, pseudocapacitive, or battery-like?, *ACS Nano*, 2018, **12**, 2081–2083, DOI: 10.1021/acsnano.8b01914.

67 A. Noori, M. F. El-Kady, M. S. Rahmanifar, R. B. Kaner and M. F. Mousavi, Towards establishing standard performance metrics for batteries, supercapacitors and beyond, *Chem. Soc. Rev.*, 2019, **48**, 1272–1341, DOI: 10.1039/C8CS00581H.

68 N. R. Chodankar, H. D. Pham, A. K. Nanjundan, J. F. S. Fernando, K. Jayaramulu, D. Goldberg, Y.-K. Han and D. P. Dubal, True meaning of pseudocapacitors and their performance metrics: Asymmetric versus hybrid supercapacitors, *Small*, 2020, **16**, 2002806, DOI: 10.1002/smll.202002806.

69 A. J. Bard and L. R. Faulkner, *Electrochemical Methods: Fundamentals and Applications*, John Wiley & Sons, Inc., New York, 2nd edn, 2001.

70 M. Bendova, F. Gispert-Guirado, A. W. Hassel, E. Llobet and A. Mozalev, Solar water splitting on porous-alumina-assisted TiO_2-doped WO_x nanorod photoanodes: Paradoxes and challenges, *Nano Energy*, 2017, **33**, 72–87, DOI: 10.1016/j.nanoen.2017.01.029.

71 A. Adan-Mas, T. M. Silva, L. Guerlou-Demourgues and M. Fatima Montemor, Application of the Mott-Schottky model to select potentials for EIS studies on electrodes for electrochemical charge storage, *Electrochim. Acta*, 2018, **289**, 47–55, DOI: 10.1016/j.electacta.2018.08.077.

72 R. Sreerung, D. Raknual, V. Vailikhit, P. Teesetsopon, N. Kitisripanya and A. Tubtimtae, Structural and electrochemical studies of undoped and In^{3+}-doped co-binary $Cu_{2-x}Te$ and Bi_2Te_3 thin films for aqueous Na–S batteries, *Ceram. Int.*, 2019, **45**, 17305–17317, DOI: 10.1016/j.ceramint.2019.05.289.

73 M. Bendova, Z. Pytlicek, J. Prasek and A. Mozalev, The growth and unique electronic properties of the porous-alumina-assisted hafnium-oxide nanostructured films, *Electrochim. Acta*, 2019, **327**, 135029, DOI: 10.1016/j.electacta.2019.135029.

74 S. Ozkan, N. T. Nguyen, I. Hwang, A. Mazare and P. Schmuki, Highly conducting spaced TiO_2 nanotubes enable defined conformal coating with nanocrystalline Nb_2O_5 and high performance supercapacitor applications, *Small*, 2017, **13**, 1603821, DOI: 10.1002/smll.201603821.

